

---


Electronic Theses and Dissertations, 2004-2019

---

2012

## Re, Os, Al And Mg Boron Rich Ceramic Compounds For Structural Application

Zhilin Xie  
*University of Central Florida*

 Part of the [Mechanical Engineering Commons](#)  
Find similar works at: <https://stars.library.ucf.edu/etd>  
University of Central Florida Libraries <http://library.ucf.edu>

This Masters Thesis (Open Access) is brought to you for free and open access by STARS. It has been accepted for inclusion in Electronic Theses and Dissertations, 2004-2019 by an authorized administrator of STARS. For more information, please contact [STARS@ucf.edu](mailto:STARS@ucf.edu).

---

### STARS Citation

Xie, Zhilin, "Re, Os, Al And Mg Boron Rich Ceramic Compounds For Structural Application" (2012).  
*Electronic Theses and Dissertations, 2004-2019*. 2173.  
<https://stars.library.ucf.edu/etd/2173>

Re, Os, Al AND Mg BORON RICH CERAMIC COMPOUNDS FOR  
STRUCTURAL APPLICATION

by

ZHILIN XIE

B.S. China University of Petroleum, 2010

A thesis submitted in partial fulfillment of the requirements  
for the degree of Master of Science  
in the Department of Mechanical, Materials and Aerospace Engineering  
in the College of Engineering and Computer science  
at the University of Central Florida  
Orlando, Florida

Spring Term  
2012

Adviser: Prof. Nina Orlovskaya  
Co-adviser: Prof. Richard G. Blair

©2012 Zhilin Xie

## ABSTRACT

Hard and ultra-incompressible materials are of great interest due to their important applications in industry. A common route to design hard materials is combining transition metals with light and small covalent elements. Light elements such as carbon, oxygen, nitrogen and boron have been considered as good candidates. This study includes the synthesis of  $\text{ReB}_2$ ,  $\text{OsB}_2$  and another higher boride  $\text{AlMgB}_{14}$ .

Most of the techniques used for  $\text{ReB}_2$  synthesis reported 1:2.5 Re to B ratio because of the loss of the B during high temperature synthesis. However, as a result of B excess, the amorphous boron, located along the grain boundaries of polycrystalline  $\text{ReB}_2$ , would degrade the  $\text{ReB}_2$  properties. Therefore, techniques which could allow synthesizing the stoichiometric  $\text{ReB}_2$  preferably at room temperature are in high demand. This thesis reported the synthesis of  $\text{ReB}_2$  powders using mechanochemical route by milling elemental crystalline Re and amorphous B powders in the SPEX 8000 high energy ball mill for 80 hours. The formation of boron and perrenic acids are also reported after  $\text{ReB}_2$  powder was exposed to the moist air environment for a twelve months period of time. The synthesized  $\text{ReB}_2$  powder was characterized by X-ray diffraction, scanning electron microscope, transmission electron microscope, secondary ion mass spectrometry and Raman spectroscopy.

$\text{OsB}_2$  also shows its attractive properties. The hardness of orthorhombic  $\text{OsB}_2$  was reported to be 37 GPa, when the applied load is lowered to 0.245N. However, only one of the three predicted phases has been synthesized. In this study, the hexagonal  $\text{OsB}_2$  has been synthesized by the mechanochemical method. The lattice parameters of the Hex- $\text{OsB}_2$  are

$\alpha=\beta=90^\circ$ ,  $\gamma=120^\circ$ ;  $a=b=2.9047 \text{ \AA}$ ,  $c=7.4500 \text{ \AA}$ . The synthesized  $\text{OsB}_2$  powder was annealed at  $1050^\circ\text{C}$  for 6 days, but no phase change was found. This shows that the Hex- $\text{OsB}_2$  is very stable.

Another promising hard material,  $\text{AlMgB}_{14}$ , was also studied in this thesis. The  $\text{AlMgB}_{14}$  was synthesized at  $1050^\circ\text{C}$  under normal pressure. Several different routes were tried and compared. It shows  $\text{AlMgB}_{14}$  cannot be synthesized merely by ball milling, which can bring the risk of oxidization. Magnesium metal is preferred to use as one of the raw materials.

*Dedicated to my family*

## ACKNOWLEDGMENTS

Thanks to my supervisor Professor Nina Orlovskaya, at the Department of Mechanical, Materials and Aerospace Engineering of University of Central Florida, for her invaluable advice, guidance and encouragement. She teaches me knowledge, experimental skills and shares her good experience. Thanks to our research group and my friends, Yan Chen, Amjad Aman, Richard Stadelmann, Maximo Navarro and Jonathan Torres. Thanks to Yaohan Chen, Gang Shao for helping me with the  $AlMgB_{14}$  synthesis.

Thanks to Professor Richard Blair. I gained a lot of skills and chemistry knowledge in his lab. He is very patient and generous, and makes me feel very comfortable in his lab. Thanks to his research group, especially David Restrepo, Jacob Todd and Justin Piedad.

Thanks to Prof. Seetha Raghavan and Prof. Jan Gou for serving as my committee members. Thanks to the staff of University of Central Florida, Department of Mechanical, Materials and Aerospace Engineering, Advanced Materials Processing and Analysis Center, Material Characterization Facility, Mr. Helge Heinrich, MCF Research Engineer, Mr. Mikhail Klimov, MCF Research Engineer, Mr. Kirk Scammon, MCF Research Engineer, Ms. Karen Glidewell, MCF Facility Coordinator, and Prof. Ghatu Subhash, University of Florida, Department of Mechanical and Aerospace Engineering, for their help with my experiments.

Above all, thanks to my family for their support and love!

The research presented in this thesis was supported by NSF 0748364 Career Award “Hard and Tough Boron Rich Ceramic Laminates Designed to Contain Thermal Residual Stresses”.

## TABLE OF CONTENTS

LIST OF FIGURES .....	ix
LIST OF TABLES .....	xi
CHAPTER 1: INTRODUCTION .....	1
CHAPTER 2: LITERATURE REVIEW .....	4
2.1 Rhenium Diboride.....	4
2.1.1 Crystal structures of ReB <sub>2</sub> .....	4
2.1.2 Synthesis of ReB <sub>2</sub> .....	5
2.1.3 Mechanical properties of ReB <sub>2</sub> .....	8
2.2 Osmium Diboride.....	9
2.2.1 Crystal structures of OsB <sub>2</sub> .....	10
2.2.2 Synthesis of OsB <sub>2</sub> .....	13
2.2.3 Mechanical Properties of OsB <sub>2</sub> .....	14
2.3 AlMgB <sub>14</sub> .....	16
2.3.1 Crystal structure of AlMgB <sub>14</sub> .....	16
2.3.2 Synthesis of AlMgB <sub>14</sub> .....	18
2.3.3 Mechanical properties of AlMgB <sub>14</sub> .....	19
2.4 Mechanochemistry.....	22
CHAPTER 3: EXPERIMENTAL PROCEDURE.....	24
3.1 Synthesis of ReB <sub>2</sub> .....	24
3.2 Synthesis of OsB <sub>2</sub> .....	25
3.3 Synthesis of AlMgB <sub>14</sub> .....	26
3.4 Characterization of ReB <sub>2</sub> , OsB <sub>2</sub> and AlMgB <sub>14</sub> .....	32
3.4.1 XRD .....	32
3.4.2 Microscopies .....	32
3.4.3 SIMS .....	33
3.4.4 Micro-Raman Spectroscopy.....	33
CHAPTER 4: RESULTS AND DISCUSSIONS .....	35
4.1 Rhenium Diboride.....	35
4.1.1 XRD .....	35
4.1.2 Microscopies .....	37
4.1.3 SIMS .....	39
4.1.4 Raman spectroscopy .....	42
4.1.5 Reaction of powder ReB <sub>2</sub> with O <sub>2</sub> and H <sub>2</sub> O .....	44
4.2 Osmium Diboride.....	45
4.2.1 XRD .....	45
4.2.2 SEM and EDX .....	50
4.2.3 TEM.....	51
4.3 AlMgB <sub>14</sub> .....	55
4.3.1 Experiment 1 .....	55
4.3.2 Experiment 2.....	58
4.3.3 Experiment 3.....	60



4.3.4 Experiment 4.....	62
CHAPTER 5: CONCLUSIONS .....	64
LIST OF REFERENCES .....	66

## LIST OF FIGURES

Figure 1: The unit cell of ReB <sub>2</sub> with Re-B and B-B bonds. [22].....	5
Figure 2: Phase diagram of the Re-B system. [23] .....	6
Figure 3: Os-B phase diagram with OsB <sub>1.1</sub> , Os <sub>2</sub> B <sub>3</sub> and OsB <sub>2</sub> phases. [35] .....	10
Figure 4: Crystal structures of (a) ReB <sub>2</sub> -type (Hex-I), (b) RuB <sub>2</sub> -type (Orth), and (c) AlB <sub>2</sub> -type (Hex-II). [18].....	11
Figure 5: Heats of formation ( $\Delta H_f$ ) at zero pressure of MB <sub>2</sub> (M=Hf, Ta, W, Re, Os, Ir). [18]....	12
Figure 6: Crystal structure of orthorhombic osmium diboride. Osmium atoms are shown as red spheres and boron atoms as yellow spheres. [3] .....	14
Figure 7: (a) The conventional unit cell of OsB <sub>2</sub> . (b) The 1×1×2 supercell showing the Os-Os layer that is strong against shear deformation in the [100] direction but weak in the [010] direction. [45].....	15
Figure 8: A layer of icosahedral in MgAlB <sub>14</sub> with extra-icosahedral atoms. The atoms shown fall within $x=\pm 1/4$ . [46] .....	17
Figure 9: Interpretation of unit cell dimensions in terms of an icosahedral arrangement. [46]....	18
Figure 10: Nose wear vs. cutting time for uncoated and coated C-2 tools in dry machining (a); Flank wear vs. cutting time for uncoated and coated C-2 tools in dry machining (b). [12] .....	21
Figure 11: (a) Spex 8000 mixer mill and (b) milling vial and media. ....	24
Figure 12: Schematic of spark plasma sintering. ....	28
Figure 13: Heating curve of spark plasma sintering. ....	28
Figure 14: The glove box and furnace. ....	30
Figure 15: (a) X-ray diffraction patterns of Re powder, (b) B powder and (c) ReB <sub>2</sub> mechanically alloyed powders after 30, 50, and 80 hours of milling. The observed broad peak at $\sim 18^\circ 2\theta$ in (b) is a common peak seen for amorphous materials. ....	36
Figure 16: SEM micrograph of ReB <sub>2</sub> powders after ball milling for 80 hours.....	38
Figure 17: (a) TEM micrograph of a particle of ReB <sub>2</sub> powder after 80 hours of milling, (b) Electron diffraction of ReB <sub>2</sub> particle, (c) TEM micrograph of ReB <sub>2</sub> lattice fringes. ....	38
Figure 18: Distribution maps of (a) Boron, (b) Rhenium, (c) Tungsten in ReB <sub>2</sub> particle obtained .....	39
Figure 19: Negative secondary ion mass spectrometry of ReB <sub>2</sub> powders after 0.5h (a, d); 40h (b, e); and 80h (c, f) milling time. ....	40
Figure 20: Positive second ion mass spectrometry of ReB <sub>2</sub> powders after 0.5h (a); 40h (b); and 80h (c) milling time. ....	41
Figure 21: Raman spectra of mechanically alloyed ReB <sub>2</sub> powders after 80 hours of ball milling. ....	43
Figure 22: X-ray diffraction patterns of ReB <sub>2</sub> powder after 1 year storage in the plastic bag without any protective atmosphere. ....	45
Figure 23: XRD patterns of Os and B mixture at different milling time. ....	47
Figure 24: Rietveld refinement XRD pattern of Os and B mixture milled for 25 hours. ....	48
Figure 25: Unit cells of hexagonal (a) and orthorhombic (b) OsB <sub>2</sub> .....	49
Figure 26: SEM of Os and B mixture milled for 14 hours. ....	50

Figure 27: EDX of the Os and B mixture milled for 14 hours. ....	51
Figure 28: Transmission electron micrograph of a particle of OsB <sub>2</sub> powder.....	52
Figure 29: Transmission electron micrograph of OsB <sub>2</sub> lattice fringes. ....	53
Figure 30: Electron diffraction pattern of OsB <sub>2</sub> particle.....	53
Figure 31: XRD pattern of annealed Os and B mixture.....	54
Figure 32: XRD pattern of AlB <sub>2</sub> , MgB <sub>2</sub> , B mixture milled for 2h, 6h, 10h and 14h.....	56
Figure 33: Heating curve of the spark plasma sintering. ....	57
Figure 34: XRD patterns of the milled mixture powder after spark plasma sintering.....	58
Figure 35: XRD patterns of Al, Mg and B mixture after milling (Ball to powder mass ratio 4:1). .....	59
Figure 36: XRD patterns of Al, Mg and B mixture after milling (Ball to powder mass ratio 10:1). .....	60
Figure 37: XRD pattern of AlMgB <sub>14</sub> . ....	61
Figure 38: XRD patterns of the powder produced by different routes in experiment 4. ....	63

## LIST OF TABLES

Table 1: Elastic moduli, Poisson's ratio and densities for the three forms of ReB <sub>2</sub> obtained from the experimentally derived elastic constants along with theoretical calculations. [27].....	9
Table 2: Density, Hardness, bulk and shear Moduli of selected superhard materials. [52].....	20
Table 3: Purity, particle size and provider of the reactants.....	26
Table 4: Information of samples prepared in Experiment 4. ....	31
Table 5: Lattice parameters of the synthesized ReB <sub>2</sub> after mechanical alloying for 30, 50 and 80 hours.....	37
Table 6: Intensity ratio of impurities to boron SIMS peaks.....	42
Table 7: Lattice parameters of the mechanochemically synthesized OsB <sub>2</sub> , simulated OsB <sub>2</sub> and ReB <sub>2</sub> . ....	49

## CHAPTER 1: INTRODUCTION

Hard and ultra-incompressible materials are of great interest due to their important applications in industry. For example, they can be coated on cutting tools, blades and pistons to reduce wear and deformation. [1] The hardest known material diamond is not appropriate to be used in cutting ferrous metal because it reacts with iron. The second hardest material c-BN is not exist naturally and must be synthesized under extremely high temperature and pressure. [2] Therefore, this motivates people search for new superhard materials.

A common route to design hard and ultra-incompressible materials is combining transition metals with light and small covalent elements. [3] Light elements such as carbon, oxygen, nitrogen and boron have been considered as good candidates. Transition-metal borides and nitrides, such as  $\text{ReB}_2$  [3],  $\text{OsB}_2$  [4,5],  $\text{PtN}_2$  [6,7],  $\text{IrN}_2$  [7] and  $\text{OsN}_2$  [8] were successfully synthesized in the recent years. Among those binary rare earth metal compounds,  $\text{ReB}_2$  and  $\text{OsB}_2$  have shown their attractive mechanical properties. For example,  $\text{ReB}_2$  and  $\text{OsB}_2$  are ultra-incompressible with bulk modulus of 365-395 GPa. [9].  $\text{ReB}_2$  was reported with maximum Vickers hardness of 48 GPa, when the applied load is 0.49N and average hardness of 31 GPa. [4]  $\text{OsB}_2$  was reported with hardness of 37 GPa, when the applied load is 0.245N. [10] After the publication of those results, some issues were raised on the indentation size effect (ISE) in hardness measurements. Although the hardness of  $\text{ReB}_2$  and  $\text{OsB}_2$  do not exceed the threshold hardness for “superhard”, 40 GPa, they are still considered as hard and ultra-incompressible materials.

Another higher boride, hard material,  $\text{AlMgB}_{14}$  was also studied in this thesis. Boron tends to form covalent bonds, but it has only three valence electrons, which are not enough for it to form three dimensional networks by covalent bonding. However, boron-rich compounds can form boron clusters to create “economic” bonding. [11] Those boron clusters are usually  $\text{B}_{12}$  icosahedra clusters. The complex interactions within (or between) those icosahedrals lead to the special mechanical and electronic properties of these materials. Those boron-rich compounds generally possess high hardness, high melting points, light weight, acid resistance and incompressibility. [11]

$\text{ReB}_2$  was reported to exhibit high hardness and low compressibility, which both are strong functions of its stoichiometry, namely Re to B ratio. Most of the techniques used for  $\text{ReB}_2$  synthesis were reported 1:2.5 Re to B ratio because of the loss of the B during high temperature synthesis. However, as a result of B excess, the amorphous boron, located along the grain boundaries of polycrystalline  $\text{ReB}_2$ , would degrade the  $\text{ReB}_2$  properties. Therefore, techniques which could allow synthesizing the stoichiometric  $\text{ReB}_2$  preferably at room temperature are in high demand.

Recently, Chen et al. predicted that orthorhombic  $\text{OsB}_2$  can be transformed to the hexagonal  $\text{OsB}_2$  under high pressure, 2.5 GPa, by local density approximation (LDA) calculation. [18] Ren et al also reported the phase transition to be 10.8 GPa by the generalized gradient approximation (GGA). [9] However, no synthesis of hexagonal  $\text{OsB}_2$  was reported, neither the phase transition pressure between those two phases. So, exploration on hexagonal  $\text{OsB}_2$  is needed.

Except the high hardness, AlMgB<sub>14</sub> has very low chemical reactivity to steel, stainless steel, and titanium even at a temperature as high as 1300°C. The coefficient of thermal expansion (CTE) of AlMgB<sub>14</sub> was measured to be  $9 \times 10^{-6} \text{ K}^{-1}$ . [12] This value is very close to the CTE of widely used materials such as steel, titanium, and concrete. It is also cheap; the projected cost of manufacture of the boride is 10% of the cost of diamond and cubic BN. The price of AlMgB<sub>14</sub> is about 0.4-2\$/g.[12] These properties make the AlMgB<sub>14</sub> to be a promising candidate to replace diamond as a high hardness material.

In this thesis, ReB<sub>2</sub> and hexagonal OsB<sub>2</sub> powders were synthesized using mechanochemical route by milling elemental powders in the SPEX 8000 high energy ball mill. The AlMgB<sub>14</sub> was synthesized at 1050 °C under normal pressure. Several different routes were tried and compared.

## CHAPTER 2: LITERATURE REVIEW

### 2.1 Rhenium Diboride

Rhenium diboride ( $\text{ReB}_2$ ) is a ceramic that has been receiving a lot of attention in the scientific community because of its unusual properties. It has been reported as a superhard material [4,13,14] with a hardness of 48 GPa measured at a small applied load (0.5N), which means  $\text{ReB}_2$  can be regarded as “superhard” materials.

#### 2.1.1 Crystal structures of $\text{ReB}_2$

It was reported that it exhibits strong and highly covalent bonding, while a strong hybridization between the Re 5d and B 2p states indicates that Re-B bonds have also prevalent covalent character with some degree of ionic bonding present [15,16,17]. Covalent boron-boron bonds are significantly stronger than the covalent Re-B bonds [18], and such difference between the B-B and Re-B bonds, as well as between nonequivalent Re-B bonds is responsible for anisotropic compressibility and rigidity of the structure [19]. The strong directional B-B bonding complimented by Re-B covalent bonds are responsible for the high resistance to elastic and plastic deformations resulting in high shear, bulk, and Young's moduli, which are indicative of high hardness of the compound [20]. It was also reported that both Re 5d and B 2p states are at the Fermi level and, hence,  $\text{ReB}_2$  exhibits metallic behavior [14].



ReB<sub>2</sub> has a hexagonal P6<sub>3</sub>/mmc (No. 194) structure with lattice parameters a=b=2.9 Å and c= 7.478 Å. Four boron atoms occupy sites (2/3, 1/3, z), (1/3, 2/3, 1/2+z), (2/3, 1/3, 1/2-z), (1/3, 2/3, 1-z) with experimental z=0.048, while two Re atoms occupy sites (1/2, 2/3, 1/4) and (2/3, 1/3, 3/4). [21] The unit cell of ReB<sub>2</sub> was shown in Figure 1. [22]

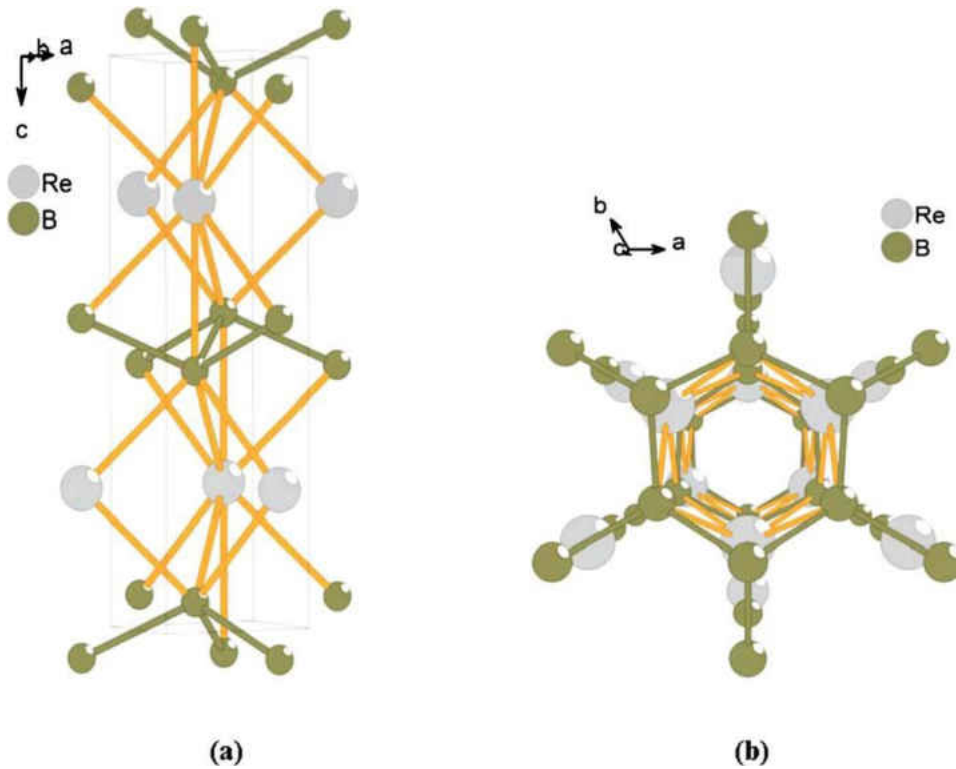


Figure 1: The unit cell of ReB<sub>2</sub> with Re-B and B-B bonds. [22]

### 2.1.2 Synthesis of ReB<sub>2</sub>

Figure 2 shows the phase diagram of the Re-B system. [23]. Although, the stoichiometric compound is ReB<sub>2</sub>, a phase of highest boron content in the Re-B phase diagram [24], it is difficult to synthesize a stoichiometric phase, and excess boron is usually required to ensure the formation of ReB<sub>2</sub> due to boron loss during the synthesis. Several approaches are reported on the

synthesis of  $\text{ReB}_2$  [4,13,14,19,20,25,26,27,24,28,29,22,30,31]. In paper [19]  $\text{ReB}_2$  was prepared using the solid state synthesis in an alumina crucible at 1300K for 4 hours in vacuum from elemental B and Re taken in a molar ratio of 2.5:1. It was reported that the synthesized material contained 5% impurity. Hexagonal platelets  $\text{ReB}_2$  crystals were synthesized using  $(\text{B}_3\text{H}_8)\text{Re}(\text{CO})_4$  molecular precursor through the confined-plume chemical deposition (CPCD) technique [28]. The precursor has a 1:3 Re/B stoichiometry, which mitigated the loss of boron during synthesis. Arc melting of the 1:2.5 ratio of elemental Re and  $^{11}\text{B}$  in Ar atmosphere was used in paper [20] to synthesize a composition of  $\text{ReB}_2$ .

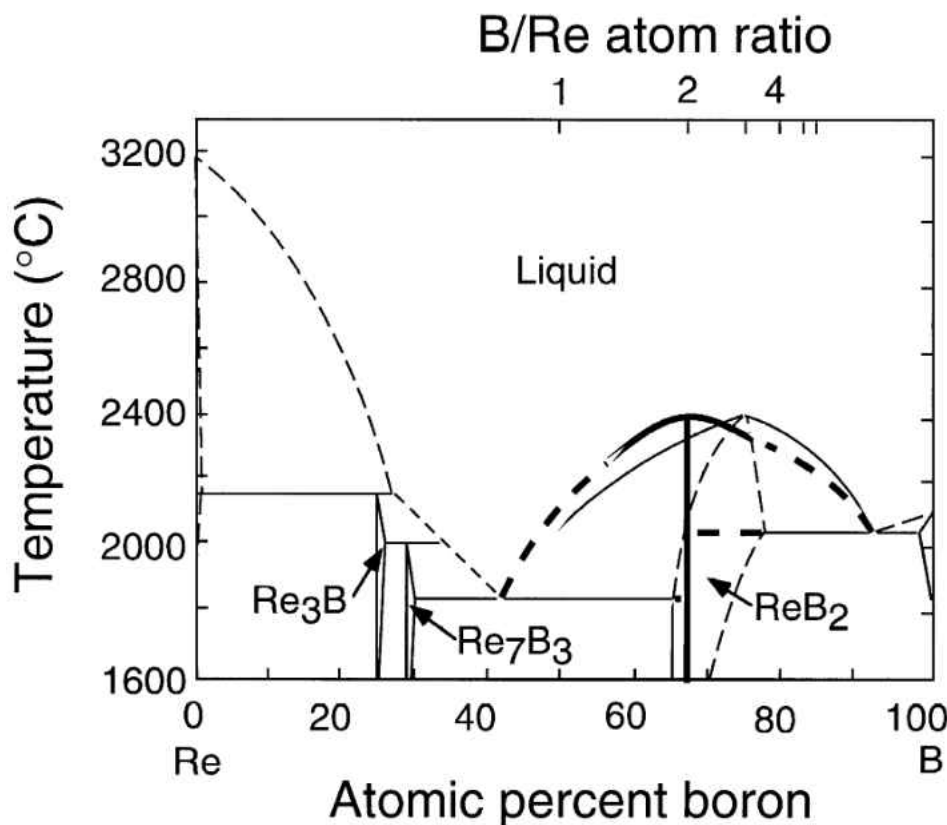


Figure 2: Phase diagram of the Re-B system. [23]

Three different techniques, all with some excess of B, were reported to be used for the synthesis of ReB<sub>2</sub>. Spark Plasma Sintering, tri-arc crystal growing technique, and arc-melting are reported as techniques of choice to produce dense ReB<sub>2</sub> [27]. Solid state synthesis from Re and B powders in Re/B molar ratio of 1:2.5 under pressure of 5 GPa and high temperature 1600°C for 60 minutes, followed by quenching to the room temperature at 100 °C/s was reported in paper [26]. ReB<sub>2</sub> crystals have also been synthesized by arc melting [4], zone melting [29] and optical floating zone furnace synthesis [25] techniques. Thin ReB<sub>2</sub> films were produced by pulsed laser deposition (PLD) technique using ReB<sub>2</sub> target, which was prepared by electron beam melting of the mixture of 1:2.5 Re to B powders [13]. While most of the techniques used to synthesize ReB<sub>2</sub> used excess boron, a few papers [14,22 ,30 ,31] utilize a 1:2 stoichiometric ratio for ReB<sub>2</sub> synthesis. In [22] two methods are reported, where one part of spectroscopically pure Re was heated with two parts of amorphous B. One method was by heating the powder mixture in sealed evacuated silica tubes at 1200°C for 12 hours and another method was by induction heating under the atmosphere of helium in vitrified alumina crucibles at 1500°C. Both methods yielded ReB<sub>2</sub> structure [22]. In [30], the 1:2 mixture of Re to crystalline <sup>11</sup>B powders were pressed into pellets, which were heated in an induction furnace under Ar atmosphere. The pellets were melted at 2600K for one hour. After synthesis, ReB<sub>2</sub> samples were ground down using a ball mill with WC milling cups and balls. The 1:2 Re to B ratio was also used for synthesis of ReB<sub>2</sub>, but with the significant presence of aluminum as the growth medium [14]. The mixture was heated to 1400°C and held at temperature for 5 hours, it was slowly cooled to 700°C and then quickly cooled to room temperature. After synthesis, the aluminum flux was dissolved in NaOH, and ReB<sub>2</sub> crystals were washed with deionized water and dried in air [14].

SPS technique was also used to sinter dense  $\text{ReB}_2$  pellets by using 1:2 Re to B powder mixture [31] but besides the  $\text{ReB}_2$  phase,  $\text{Re}_7\text{B}_3$  phase along with C impurity was also obtained during sintering. All the described techniques, used for the synthesis of  $\text{ReB}_2$ , involved using of high temperatures, sometimes as high as 2600K. Since the vapor pressure of boron is much higher than that of rhenium, it created a problem with the stoichiometry of the  $\text{ReB}_2$  compound. A technique for  $\text{ReB}_2$  synthesis at nominally room temperature would represent a major advance in the material's manufacture. The discussion in the literature inspired us to examine a new synthetic route to  $\text{ReB}_2$  powders. These powders, as well as those of other boron-rich solids are typically not commercially available; therefore, techniques which allow synthesis of boron-rich solids are of high interest, especially if synthesis is performed at room or near room temperatures.

### 2.1.3 Mechanical properties of $\text{ReB}_2$

There have been numerous discussions in regard to the actual hardness of  $\text{ReB}_2$  which was reported in Science [4]. Several reports [32,25,26] suggest that the hardness of  $\text{ReB}_2$  was overestimated since it was measured in the region where the indentation size effect (ISE) is known to exist. According to different studies [32,25,26] the hardness value for  $\text{ReB}_2$  lies well below the threshold of 40 GPa, and claims of  $\text{ReB}_2$  being a super-hard material cannot be justified. However, evidence was produced [27] that the measured mechanical properties are strongly compositional dependent, where Re to B stoichiometry as well as morphology of the grains plays important roles in the mechanical behavior of  $\text{ReB}_2$ . In particular, the presence of

excess of amorphous boron along the grain boundaries of spark plasma sintered  $\text{ReB}_2$ , where 1:2.5 Re to B stoichiometric ratio was used to synthesize polycrystalline material, was responsible for the measured lower hardness and Young's modulus values [27]. Table 1 shows the elastic moduli for the tri-arc crystal, SPS compact, arc-melted  $\text{ReB}_2$  and theoretical models. The tri-arc crystal shows the highest elastic moduli, which is closer to the theoretical results. [27]

Table 1: Elastic moduli, Poisson's ratio and densities for the three forms of  $\text{ReB}_2$  obtained from the experimentally derived elastic constants along with theoretical calculations. [27]

	$E(\text{GPa})$	$B(\text{GPa})$	$G(\text{GPa})$	$\nu$	$P(\text{g/cm}^3)$
Tri-arc	661	383	273	0.21	12.51
SPS compact	434	230	183	0.19	10.89
Arc-melted	614	296	267	0.15	11.12
GGA approx.	683	355	289	0.18	12.96

Another problem, which makes  $\text{ReB}_2$  very difficult material to work with, is that it slowly degrades in the presence of moist air. When  $\text{ReB}_2$  interacts with water in air it becomes covered with a viscous solution within a few months. This property becomes especially serious when high surface area powders are exposed to water vapors in air, which may complicate  $\text{ReB}_2$  implementation in industrial applications.

## 2.2 Osmium Diboride

Osmium is the most incompressible metal with bulk modulus ranges between 395 to 462 GPa, which is comparable to diamond (443 GPa). [33][34] Since osmium carbide is metastable under ambient condition and osmium nitride only can be synthesized under extreme conditions

(greater than 50GPa and 2000K), osmium boride may be a good choice. Os-B system contains  $\text{OsB}_{1.1}$ ,  $\text{OsB}_3$  and  $\text{OsB}_2$ , among which  $\text{OsB}_2$  has more Os-B bonds and results in higher hardness.

[10] The phase diagram of Os-B system is shown in Figure 3. [35]

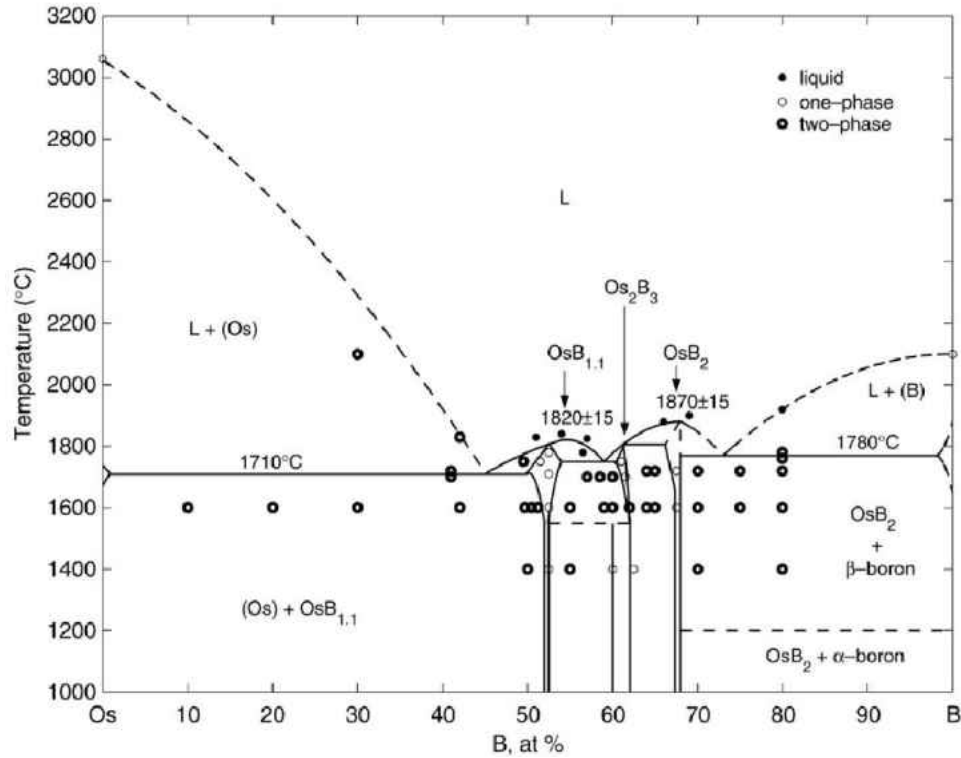


Figure 3: Os-B phase diagram with  $\text{OsB}_{1.1}$ ,  $\text{Os}_2\text{B}_3$  and  $\text{OsB}_2$  phases. [35]

### 2.2.1 Crystal structures of $\text{OsB}_2$

Both  $\text{OsB}_2$  and  $\text{ReB}_2$  are ultra-incompressible and hard materials. However,  $\text{OsB}_2$  and  $\text{ReB}_2$  own different crystal structures. So far all the synthesized  $\text{OsB}_2$  [3,10,36,37,30] has an orthorhombic  $Pmmn$  (No. 59) structure with lattice parameters  $a=4.6855(6)$  Å,  $b=2.8730(3)$  Å and  $c=4.0778(4)$  Å [36], while  $\text{ReB}_2$  has a hexagonal  $P6_3/mmc$  (No. 194) structure with lattice

parameters  $a=2.9 \text{ \AA}$  and  $c=7.478 \text{ \AA}$  [4]. In the orthorhombic  $\text{OsB}_2$  unit cell, two Os atoms are placed at Wyckoff position of  $2a (1/4, 1/4, z)$  and  $4f (u, 1/4, v)$  for B atoms. [38, 39] Hexagonal  $\text{OsB}_2$  has the same symmetry with  $\text{ReB}_2$  [40]. The hexagonal unit cell contains two  $\text{OsB}_2$  chemical formula unit (f.u.), two Os atoms are placed in  $2c (1/3, 1/3, 1/4)$  and four B atoms in  $4f (1/3, 2/3, z)$  positions, with  $z=0.548$ . [9]

According to Chen's study on 5d transition metal diborides  $\text{MB}_2$  ( $M=\text{Hf, Ta, W, Re, Os, Ir}$ ), there are 3 types of crystal structures for  $\text{OsB}_2$ , as shown in Figure 4,  $\text{ReB}_2$ -type (Hex-I),  $\text{RuB}_2$ -type (Orth), and  $\text{AlB}_2$ -type (Hex-II). So far, the synthesized  $\text{OsB}_2$  has a  $\text{RuB}_2$ -type (Orth) structure, whereas  $\text{ReB}_2$  crystallizes in the hexagonal  $\text{ReB}_2$ -type structure. As shown in Figure 5, the Hex-I and Orth structures are very close in energy for all  $\text{MB}_2$  compounds. The Orth structure becomes marginally more stable than Hex-I, and Hex-II is the least stable for  $\text{OsB}_2$ . So, Hex-I structure maybe a pressured-induced phase for  $\text{OsB}_2$ . [18]

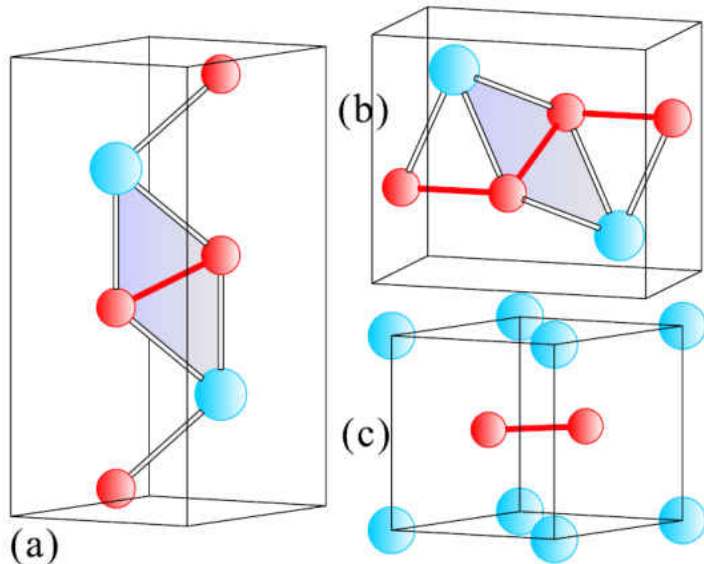


Figure 4: Crystal structures of (a)  $\text{ReB}_2$ -type (Hex-I), (b)  $\text{RuB}_2$ -type (Orth), and (c)  $\text{AlB}_2$ -type (Hex-II). [18]

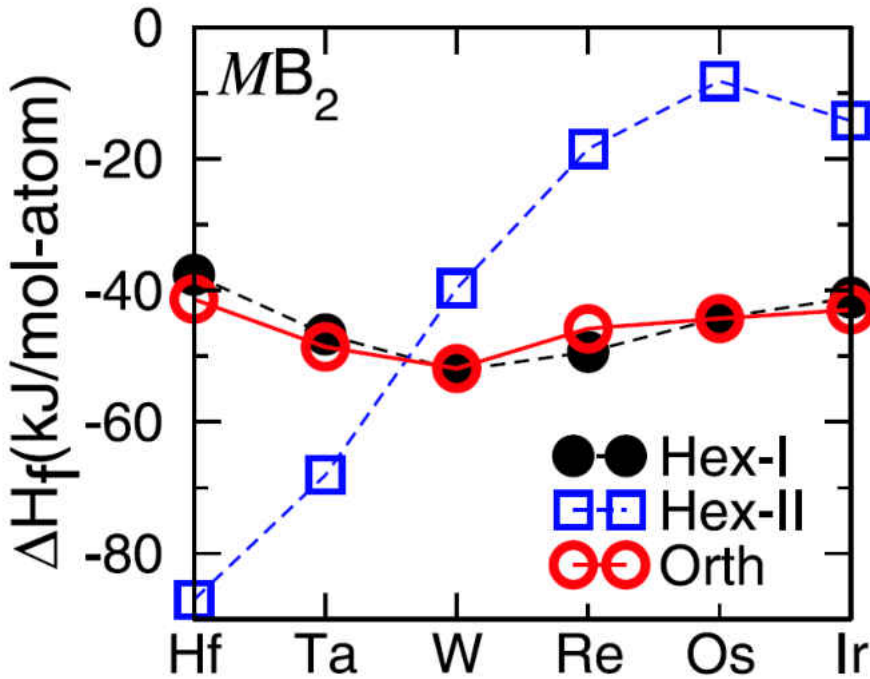


Figure 5: Heats of formation ( $\Delta H_f$ ) at zero pressure of  $MB_2$  ( $M=Hf, Ta, W, Re, Os, Ir$ ). [18]

A generalized gradient approximation (GGA) calculation was done by Ren et al. The GGA calculation results agree with the previous theoretical results and the experimental ones. The hexagonal structure is only 0.048 eV higher than the orthorhombic structure at zero pressure, and the transition pressure of orthorhombic structure to hexagonal structure is 10.8 GPa. [9]

However, Chen et al. reported that the orthorhombic  $OsB_2$  was found to transfer into hexagonal structure at 2.5 GPa with the local density approximation (LDA). [18] To our knowledge, there is no experimental report about the transition pressure of  $OsB_2$ . This motivates us to verify it by experiments, but the first step is to explore the Hex-I  $OsB_2$ .



### 2.2.2 Synthesis of OsB<sub>2</sub>

The orthorhombic OsB<sub>2</sub> was first synthesized in 1960s, but its high hardness was just found recently by Cumberland et al. in 2004. [3] Two methods were employed in their synthesis. When considered osmium metal can be oxidized to an extremely hazardous compound osmium tetroxide, vacuum or inert atmosphere was used to prevent oxidization in both methods. In the first method, MgB<sub>2</sub> was used as precursor in solid-state metathesis reactions. [41] The reactants OsCl<sub>3</sub> and MgB<sub>2</sub> were mixed with a ratio of 2:3, initiated with a resistively heated Nichrome wire, self-propagated and went to completion in less than 1s, then Os<sub>2</sub>B<sub>3</sub>, OsB forms and some Os and B left. In the second method, a 1:2 molar ratio of Os:B heated at 1000 °C yielded a mixture of osmium borides; while the Os and B powders are mixed with 1:5 molar ratio and heated at 1000 °C for 3 days, then pure OsB<sub>2</sub> forms and some boron left. [3]

Another synthesis experiment was done by Singh. Single crystals of OsB<sub>2</sub> were grown with a high temperature solution growth method using Cu-B as the flux. First, arc-melt Os powder and B chunks mixture with stoichiometric ratio, and put the arc-melted OsB<sub>2</sub> sample in an Al<sub>2</sub>O<sub>3</sub> crucible. The crucible was put into a tube furnace which was protected by argon flow. Heat the furnace to 1450 °C in 6 hours and hold this temperature for 6 hours. After it was cooled down, dissolve the Cu-B flux by dilute nitric (HNO<sub>3</sub>) acid. [36]

### 2.2.3 Mechanical Properties of OsB<sub>2</sub>

The incompressibility (bulk modulus) of a wide variety of substances can be directly correlated with their valence electron densities, electrons/Å<sup>3</sup>. [42] Since high bulk modulus is often correlated with hardness, maximizing the valence electron density is a potentially useful design parameter. [43,44] Osmium has one of the highest valence electron densities for a pure metal (0.572 electrons/Å<sup>3</sup>), and recent measurements of its bulk modulus give values in the range of 395-462 GPa. [33,34,35,] However, osmium has metallic bonds, whereas diamond possesses covalent bonds. This is why the bulk moduli of diamond and osmium are very close, but their hardnesses vary greatly. [3]

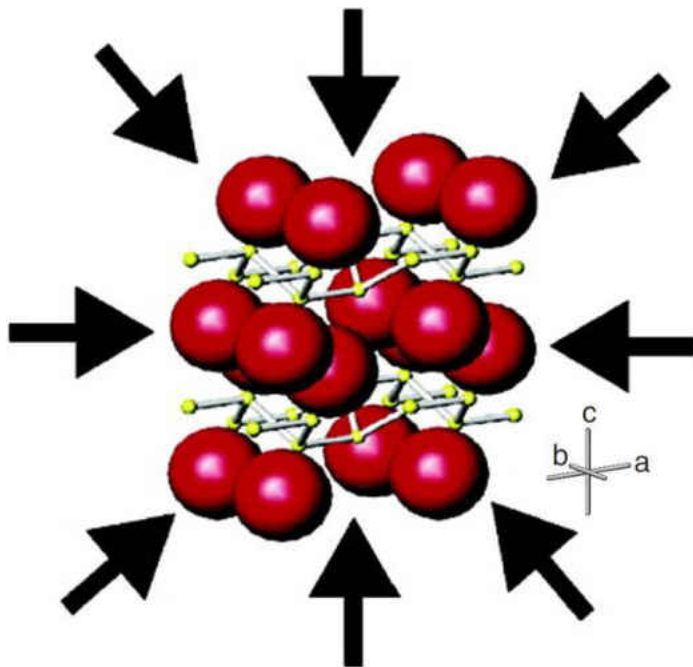


Figure 6: Crystal structure of orthorhombic osmium diboride. Osmium atoms are shown as red spheres and boron atoms as yellow spheres. [3]

By incorporating boron atoms into osmium metal to create covalent bonding, the hardness can be improved. The individual axes changes linearly with increasing pressure. However, the compression of the axes shows interesting anisotropy, which is because  $\text{OsB}_2$  unit cell is not cubic. Figure 6 shows the crystal structure of orthorhombic  $\text{OsB}_2$ . The b-direction of the crystal is most compressible, while the c-direction is the least compressible. [3]

Figure 7 shows the conventional unit cell of orthorhombic  $\text{OsB}_2$ . In Figure 1a, a  $1 \times 1 \times 2$  supercell highlighting the weak (001) Os-Os layer, formed by the Os1 and Os2 atoms in the adjacent unit cells (Figure 1b). The triangular structure B1-Os1-B2 (or B3-Os2-B4) in the unit cell strengthens this Os-Os layer against the shear deformation in the [100] direction; however, in the [010] direction, the Os-Os layer is weak under the shear stress because most of the B-Os bonds are either perpendicular to this direction or lying outside of this Os-Os layer. [45].

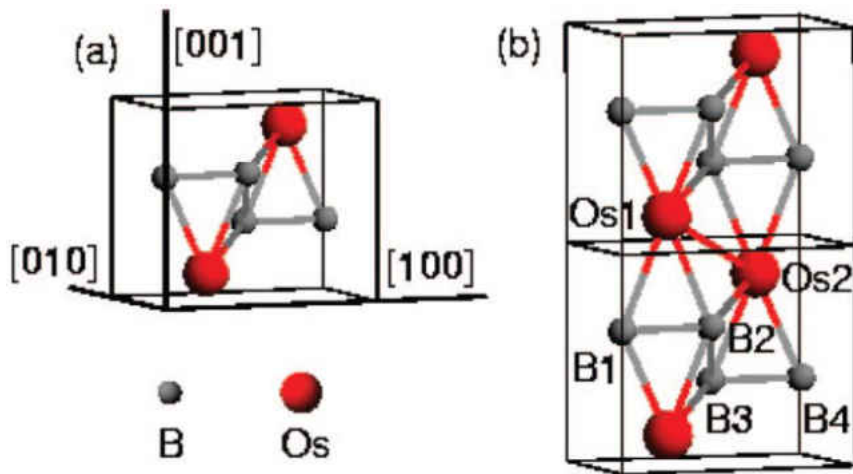


Figure 7: (a) The conventional unit cell of  $\text{OsB}_2$ . (b) The  $1 \times 1 \times 2$  supercell showing the Os-Os layer that is strong against shear deformation in the [100] direction but weak in the [010] direction. [45]

The Mohs hardness of the  $\text{OsB}_2$  is 9 on the Mohs scale (diamond is 10), which is comparable to sapphire. [3] The Vicker's hardness is 37 GPa, when the applied load is lowered to 0.245N. Also, the hardness was found to be orientationally dependent, with values obtained along the  $\langle 100 \rangle$  direction higher than those along the  $\langle 001 \rangle$  direction, because the stronger B-B bonds located along the  $\langle 100 \rangle$  direction. The Young's modulus was found to be  $410 \pm 35$  GPa by nanoindentation experiments. [10]

## 2.3 AlMgB<sub>14</sub>

### 2.3.1 Crystal structure of AlMgB<sub>14</sub>

The crystal structure of AlMgB<sub>14</sub> was determined by Matkovich et al. in 1969. As shown in Figure 8, the distance between intra-icosahedral boron-boron with an average of 1.810 Å. There is a larger distance of 2.040 Å between extra-icosahedral boron atoms. Magnesium has 12 bonds to boron atoms in six different icosahedral at an average distance of 2.730 Å and two bonds to extra-icosahedra boron neighbors at a distance of 2.363 Å. Aluminum has eight bonds to atoms in four different icosahedra at an average distance of 2.37 Å and four extra-icosahedra boron atoms at a short distance of 2.061 Å. [46]

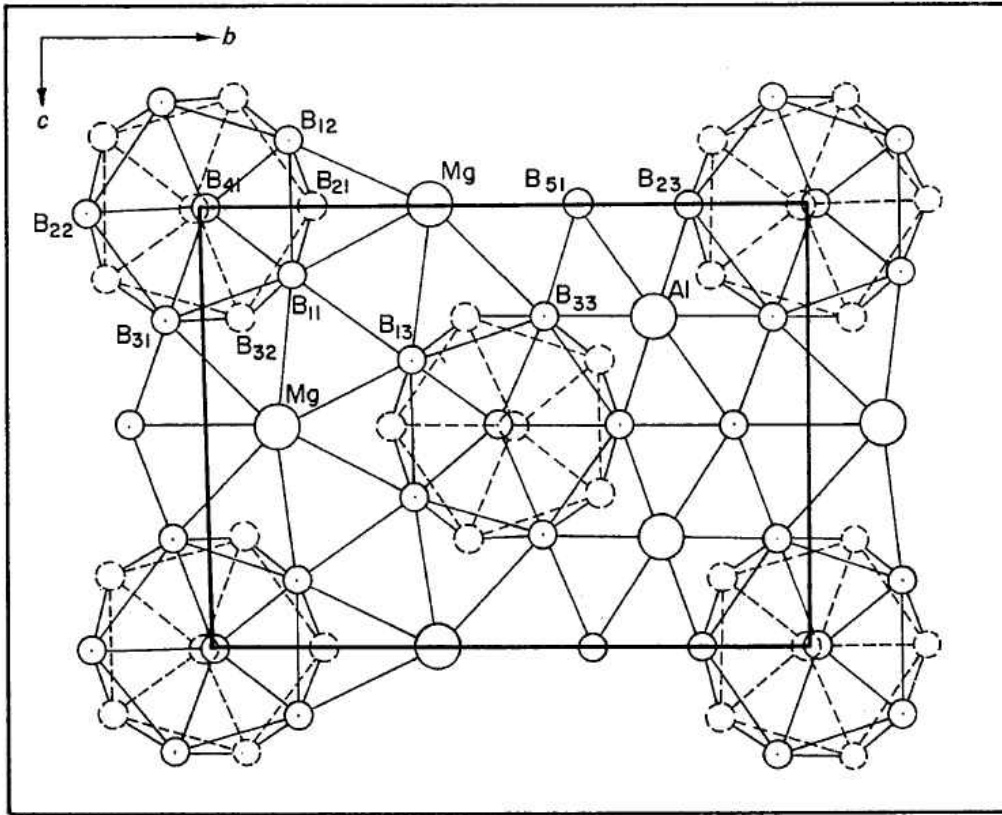


Figure 8: A layer of icosahedral in  $\text{MgAlB}_{14}$  with extra-icosahedral atoms. The atoms shown fall within  $x=\pm 1/4$ . [46]

The  $\text{AlMgB}_{14}$  has an orthorhombic structure with 64 atoms. The icosahedrons are arranged in distorted, closed-packed layers, with atoms between the icosahedra. The lattice parameters of  $\text{AlMgB}_{14}$  was found  $a=5.848 \text{ \AA}$ ,  $b=10.313 \text{ \AA}$ ,  $c=8.115 \text{ \AA}$  and  $\beta=90^\circ$ . Figure 9 shows the arrangement of boron icosahedra in unit cell. [46] Crystallographic studies indicate that the metal sites are not fully occupied in the lattice. The actual formula of  $\text{AlMgB}_{14}$  may be close to  $\text{Al}_{0.75}\text{Mg}_{0.78}\text{B}_{14}$ .

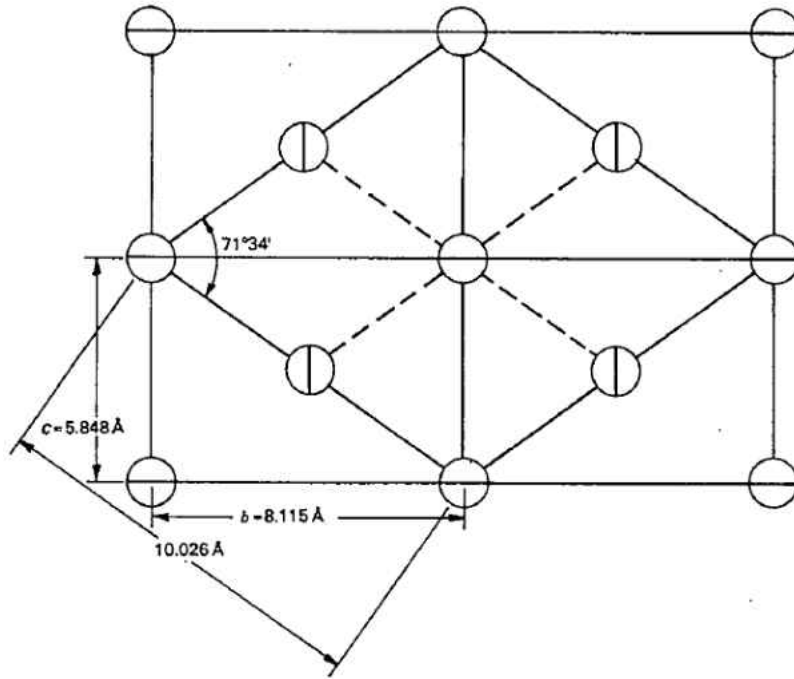


Figure 9: Interpretation of unit cell dimensions in terms of an icosahedral arrangement. [46]

### 2.3.2 Synthesis of AlMgB<sub>14</sub>

AlMgB<sub>14</sub> was first synthesized by Matkovich et al. by accident in 1969. AlMgB<sub>14</sub> was observed when the mixture of boron and aluminum was heated to 1000 to 1400 °C, and Mg was impurity. Later, larger amount of the AlMgB<sub>14</sub> was prepared by heating a mixture of magnesium, aluminum and boron with a proportion of 1: 2: 14. The mixture was heated to 900 °C for six hours; cooled and treated with concentrated hydrochloric acid. [46] After that, different synthesis methods were used to get high quality AlMgB<sub>14</sub> samples.

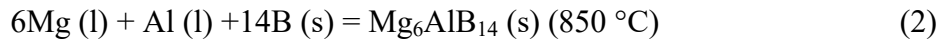
The MA/hot uniaxial pressing technique was used by Lewis et al. in their synthesis of AlMgB<sub>14</sub>. [47] The reactive sintering of the hard boride AlMgB<sub>14</sub> from the elements was

investigated using the pulse electric current sintering (PECS) method. [48] No  $\text{AlMgB}_{14}$  was formed during the milling. Also, it was found that vacuum annealed boron brings better results than the untreated one and boron pieces are less oxygen contaminated, which leads to the most pure product in the group. When sintered under lower temperature,  $\text{AlMgB}_4$  was found, with increasing sintering temperature,  $\text{AlMgB}_4$  turns to  $\text{AlMgB}_{14}$ . So, Roberts suggested that the reaction



maybe happened.

Kevorkijan et al. successfully synthesized  $\text{AlMgB}_{14}$  under normal pressure and high temperature by using magnesium as a precursor. [49] Recently, Sun et al. applied a two-step heat treatment on the phase formation of  $\text{AlMgB}_{14}$ . This method based on the two reactions below.



Mix Mg, Al and B with stoichiometric ratio of  $\text{Mg}_6\text{AlB}_{14}$  uniformly by hand grinding in glove box filled with argon gas. The samples are sintered at 850 °C for 3 hours in closed argon atmosphere. In the second step, the  $\text{Mg}_6\text{AlB}_{14}$  disks were put in the vacuum furnace sintered around 1050 °C for 180min yields 84% of  $\text{AlMgB}_{14}$ . [50]

### 2.3.3 Mechanical properties of $\text{AlMgB}_{14}$

One of the most interesting properties of  $\text{AlMgB}_{14}$  is its high hardness. Materials with high hardness and thermodynamically stable are usually considered to be used for tool and

protective coating applications. Some mechanical properties of hard materials are listed in Table 2 for comparison. It can be seen that the hardness of TiB<sub>2</sub> doped AlMgB<sub>14</sub> is comparable to the cubic BN and cubic C<sub>3</sub>N<sub>4</sub>; while the density is lower than that of diamond, BN and C<sub>3</sub>N<sub>4</sub>.

Table 2: Density, Hardness, bulk and shear Moduli of selected superhard materials. [52]

Materials	Density (g/cm <sup>3</sup> )	Hardness (Gpa)	Bulk Modulus (GPa)	Shear Modulus (GPa)
C (diamond)	3.52	70	443	535
BN (cubic)	3.48	45-50	400	409
C <sub>3</sub> N <sub>4</sub> (cubic)	N/A	40-55	496	332
TiB <sub>2</sub>	4.5	30-33	244	263
AlMgB <sub>14</sub>	2.66	32-35	N/A	N/A
AlMgB <sub>14</sub> +Si	2.67	35-40	N/A	N/A
AlMgB <sub>14</sub> +TiB <sub>2</sub>	2.7	40-46	N/A	N/A

Higashi et al. reported a hardness value of 27.4 to 28.3 GPa for AlMgB<sub>14</sub>. [51] Cook et al. obtained a hardness value of 32 to 35 GPa for their synthesized AlMgB<sub>14</sub> baseline material, which is much higher than the hardness reported by other investigators who grew AlMgB<sub>14</sub> single crystals from high temperature solutions. When dope the baseline AlMgB<sub>14</sub> with 30 percent of TiB<sub>2</sub>, the hardness increased greatly to 46 GPa, which makes this material belongs to the category of “superhard material”. [52] Also, it is found that 30 percent of doping makes AlMgB<sub>14</sub>-TiB<sub>2</sub> show the highest hardness. In most of the hard materials, hardness decreased when adding other elements of compounds. However, AlMgB<sub>14</sub> shows is absolutely the opposite, which is interesting but hard to explain.



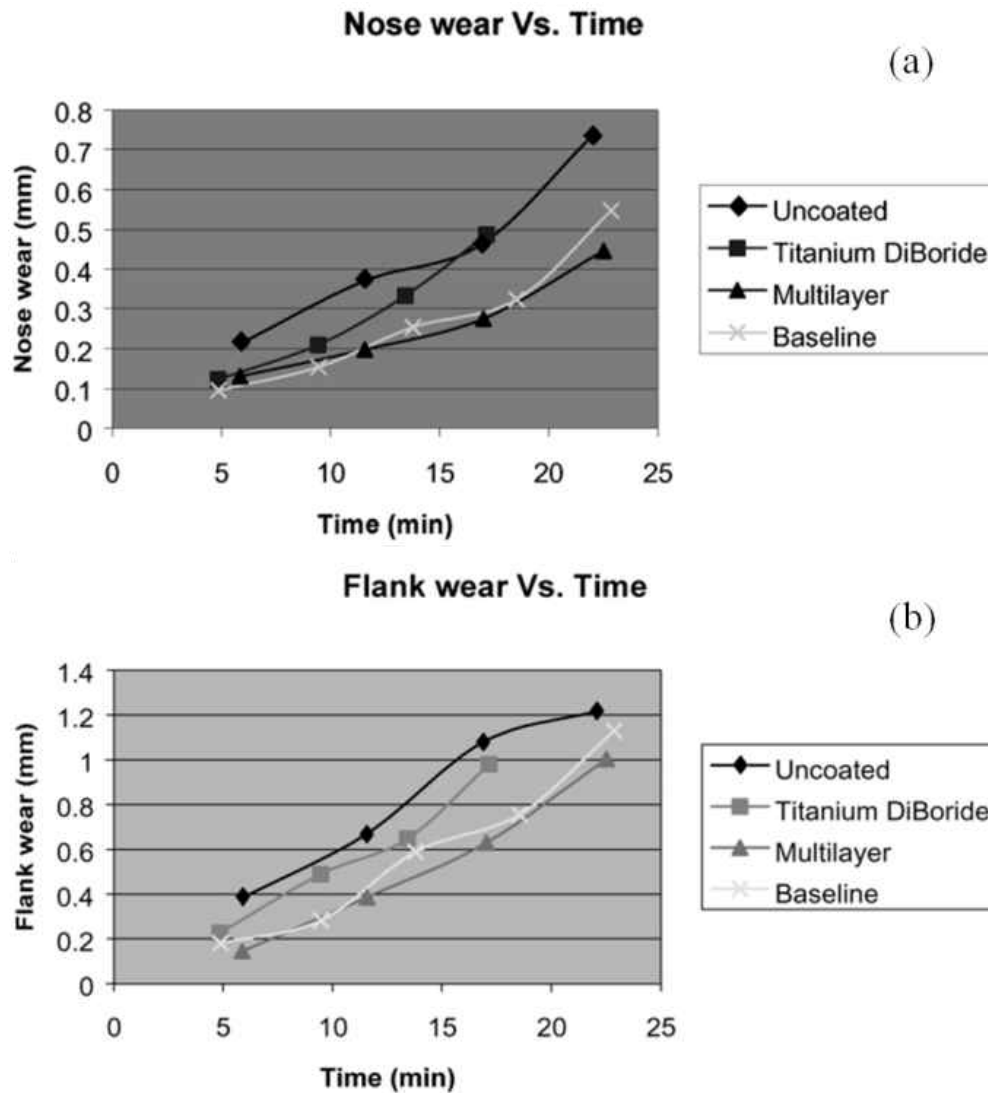


Figure 10: Nose wear vs. cutting time for uncoated and coated C-2 tools in dry machining (a); Flank wear vs. cutting time for uncoated and coated C-2 tools in dry machining (b). [12]

Cherukuri et al have successfully coated AlMgB14 on C-2 and C-5 tools by Pulsed Laser Deposition (PLD). Thin coatings are strongly adhered to the tool edges at low temperature (500 °C). In Figure 10, it is also demonstrated that AlMgB14 has the potential to exceed the performance of Ti-based coatings. [12]

## 2.4 Mechanochemistry

Mechanochemistry is a part of solid state chemistry where intra-molecular bonds are mechanically broken. [53] Solids are different from gases and liquids, it can support shear strain. Thus mechanical forces can trigger chemical reactions. Shear force is more effective than pure isotropic compression, because shear changes the symmetry of a solid or molecule. For example, sheared spheres turned to be ellipsoids, cubic symmetry becomes tetragonal. The electronic structure of bonds in solids becomes unstable after the breaking of symmetry, which makes the solid tend to have chemical reaction. [54] Large strain brings together the highest occupied molecular orbital (HOMO) and the lowest unoccupied molecular orbital (LUMO) to close the gap. Then the bonding electrons delocalize into the anti-bonding states. Electrons move freely and the activation energy for the reaction becomes zero, which is called athermal reaction. [55]

Gilman et al. used a square lattice as a 2D model to compare the effect of shear and isotropic compression. When the square lattice is applied with a hydrostatic strain, the shifts of the band gap mid-point will be the same in the two orthogonal directions, and the minimum band gap will not be changed. [55] However, when the square lattice is applied with a shear strain, it causes one axis increase and the other decrease and the band gap mid-point shift in opposite directions. Thus the minimum gap decreased. [55]

Ball milling is a widely used technique in mechanochemical synthesis. It contains planetary, vibration devices, Spex mills. Mechanical actions occur due to both normal pressure and shear. Based on the construction features of a mill and its operation regime, the relation between pressure and shear can be varied in a wide range. [56]

Besides, ball milling accelerates the kinetics of chemical reactions by creating fresh interfaces between reacting phases by dynamic fracturing, deformation and cold welding of the solid particles. It is also reported that milling devices can be used to synthesize a variety of metastable phases, amorphous alloys and nanostructured compounds. [57] In paper [58], discrete element models of the milling process were generated using EDEM. It is reported that Spex shake mill can produce compressive force 0.4 to 3 GPa by using steel milling vials and balls.

## CHAPTER 3: EXPERIMENTAL PROCEDURE

### 3.1 Synthesis of ReB<sub>2</sub>

Rhenium metal powder (99.99% pure, -325 mesh; Cerac) and boron powder (99% pure, -325 mesh, amorphous; Alfa Aesar) were used as received. A total of 20 grams of a stoichiometric amount of rhenium and boron powders were loaded into a Spex tungsten carbide vial with two 12.7mm diameter tungsten carbide balls. The grinding was done by a Spex 8000 mixer mill for a total of 80 hours.



Figure 11: (a) Spex 8000 mixer mill and (b) milling vial and media.

Figure 11 shows the Spex 8000 mixer mill, milling vial and media. After ball milling, the powders were stored in plastic bags. No protective atmosphere was used in the whole experiment.

### 3.2 Synthesis of OsB<sub>2</sub>

In order to experimentally explore the hexagonal phase of OsB<sub>2</sub> and find the phase transition pressure, experiments were conducted using ball milling. [59,60] This approach allows synthesis of numerous novel materials and very complex compounds by applying mechanical force to mixtures of elemental powders [56]. It involves repeated cold welding, fracturing, and re-welding of powder particles due to heavy deformation. As a result, the microstructure gets refined and the increased diffusivity (due to creation of a high density of crystalline defects) and reduced diffusion distances (due to refinement of microstructure) allow synthesis to take place at or near room temperature. In a mechanochemical synthesis, attrition results in the reduction of particle size. This effectively creates micro reaction regimes where frictional heating can supply the activation energy for the production of line compounds from the elements. At this point, the heat of reaction can drive the reaction forward and even result in a self-propagating reaction [61]. This method has been used to produce intermetallic phases, metallic glasses and composites and different borides [59,60 ,62,63,64,65,66,67]. Among the mechanochemical approaches, ball milling is a convenient way to achieve high pressure with shear forces.

Osmium metal powder (99.95% pure, Heraeus) and boron powder (99% pure, -325 mesh, amorphous and crystalline; Alfa Aesar) were used. Osmium and boron powders with molar ratio of 1:3, and two 12.7mm diameter tungsten carbide balls were loaded into a Spex tungsten carbide vial. The ball-to-powder weight ratio was 4:1. The grinding was done by a Spex 8000 mixer mill for a total of 33 hours. Samples were taken out for XRD by every 2 hours. After milling, the mixture powder was sealed in a small vacuum quartz tube, and heated in a furnace for 6 days at 1050 °C.

### 3.3 Synthesis of AlMgB<sub>14</sub>

Different ways were used in synthesizing of AlMgB<sub>14</sub>. The processes of loading powders in all experiments were done in glove box under argon atmosphere (with an average oxygen concentration of 0.45 ppm), except the step of loading powders to SPS dies in Experiment 1. Table 3 listed the information of all the powders used in the experiments.

Table 3: Purity, particle size and provider of the reactants.

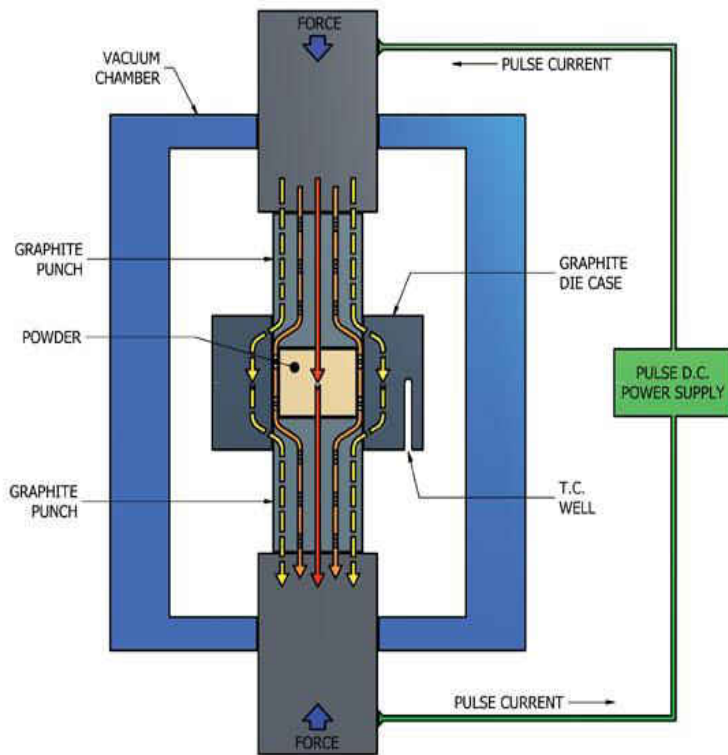
Reactants	purity	particle size	company
Al	99.97%	-325 mesh	Materion
Mg	99.80%	-325 mesh	Alfa Aesar
AlB <sub>2</sub>	99%	-325 mesh	Alfa Aesar
MgB <sub>2</sub>	99%	-325 mesh	Alfa Aesar
B	99%	-325 mesh	Alfa Aesar
B	90-92%	<5micron	Materion

## Experiment 1

The reaction



was supposed to be realized to produce  $\text{AlMgB}_{14}$ . Ball milling was first used to mix all the powders homogeneously and activate the reaction. The stoichiometric amount of  $\text{AlB}_2$  (99%, -325 mesh, Alfa Aesar),  $\text{MgB}_2$  (99%, -325 mesh, Alfa Aesar), B (99%, -325 mesh, Alfa Aesar) and two tungsten carbide balls (12.7 mm diameter) were loaded into a Spex tungsten carbide vial. The ball to powder mass ratio was 4:1. The vial was loaded on Spex 8000 mixer mill for 23.5 hours. In order to find out if  $\text{AlMgB}_{14}$  can be synthesized by ball milling, samples were taken out for XRD every 4 hours of milling. After milling, powders were loaded in 20mm diameter graphite dies for Spark Plasma Sintering (SPS). This process was exposed in air with a short time. Different from conventional hot pressing, heat generated internally in SPS. Figure 12 shows the general schematic of the SPS. DC current passes through graphite die and sample when the sample is conductive. The sintering was under 1450 °C and 50 MPa, lasted for 5 minutes. The heating curve of the whole sintering was shown in Figure 13. An 8mm thick disk was obtained after sintering. The disk was ground into powder again for XRD.



Source: [http://www.ceramicindustry.com/CI/Home/Images/ci0508\\_f5\\_fig2\\_lrg.jpg](http://www.ceramicindustry.com/CI/Home/Images/ci0508_f5_fig2_lrg.jpg)

Figure 12: Schematic of spark plasma sintering.

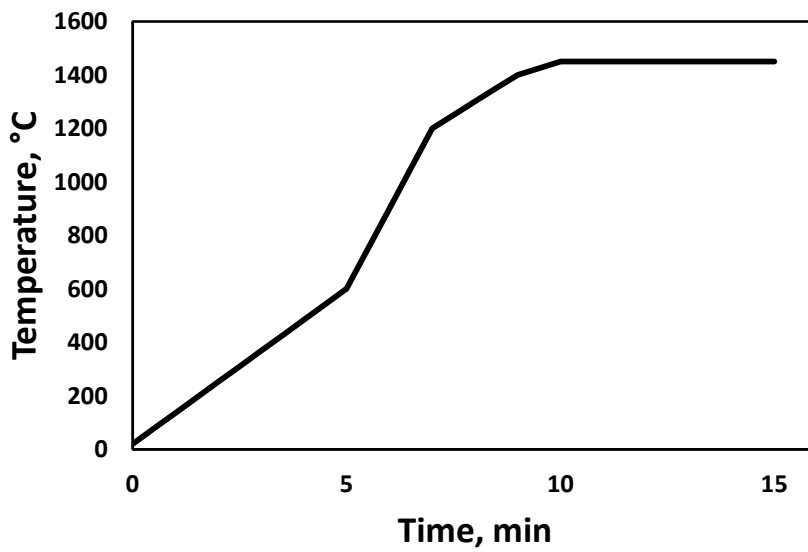
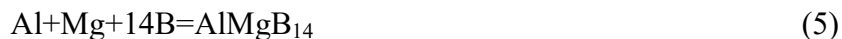


Figure 13: Heating curve of spark plasma sintering.



## Experiment 2

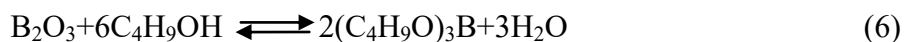
The synthesis approach was changed to base on the reaction



since the elemental reactants may be more reactive. Al (99.97% pure, -325 mesh, Materion), Mg (99.8% pure, -325 mesh, Alfa Aesar) and B (99% pure, -325 mesh, amorphous and crystalline, Alfa Aesar) powders were loaded into vial stoichiometrically. They were milled for a total of 40 hours. The ball to powder mass ratio was 4:1. Samples were taken out every 10 hours of milling for XRD. Another part of the mixture powders were milled with a ball to powder mass ratio of 10:1 and milled for 2 hours. The milled powders were sintered in a tube furnace for 2 hours under argon flow. The sintering temperature was 1050 °C.

## Experiment 3

Oxidization leads to the failure in the first two experiments. This experiment is aim to solve the problem of oxidization. The oxygen source can also be the boron powder since the high surface ratio powder can be oxidized somehow. Butanol was used to purify the boron powder. In the reaction



the boiling point of  $\text{C}_4\text{H}_9\text{OH}$  is 118 °C which is higher than the boiling point of water. After it is fully reacted, the mixture was heat to 110°C to remove water. By the same time, the reaction will be forced to react towards right hand side so that more  $\text{B}_2\text{O}_3$  will be consumed. Finally, the mixture was centrifuged and dried.

When considered the magnesium powder is volatile at high temperature, excess magnesium was used in this experiment. The elemental Al (99.97% pure, -325 mesh, Materion),

Mg (99.8% pure, -325 mesh, Alfa Aesar) and boron (92% pure, -325 mesh, amorphous, Materion) powders were mixed in a molar ratio of 1:6:14. Instead of grinding the powders in Spex ball mill, mortar and pestle were used to mix those powders in a glove box. By this way, the mixture may not be as homogeneous as that grinded by Spex ball mill, but it avoided the risk of oxidization. The mixed powder was pressed to pellets (10mm diameter and 5mm thickness) by a small die in the glove box, as shown in Figure 14.



Figure 14: The glove box and furnace.

By pressing powders together, diffusion of atoms under high temperature can mitigate the problem of inhomogeneous mixing. The pellets were put into a steel boat and sent to the tube furnace. All the preparing steps were in argon atmosphere. The furnace was heated up to 1050°C in 4 hours, maintain 1050 °C for 3 hours and then cooled down to room temperature in 5 hours. Argon flow was maintained during sintering. The pressure in the tube was a little higher than air pressure to prevent air going into the tube. After sintering, a pellet was ground for powder XRD.

#### Experiment 4

Experiment 4 was attempted to compare the different synthesizing routes. Table 4 listed the difference of each route. The same method was used as described in Experiment 3. Six samples were prepared and sintered in the same batch. XRD was performed after sintering. When considered the high vapor pressure of Mg leads to Mg loss during sintering, excess of Mg was used in Route 2.

Table 4: Information of samples prepared in Experiment 4.

Routes	reaction equations	Sintering
1	$Mg+Al+14B=AlMgB_{14}$	3 hours at 1050 °C
2	$6Mg+Al+14B=AlMgB_{14}$	3 hours at 1050 °C
3	$Mg+Al+14B=AlMgB_{14}$	6 hours at 1050 °C
4	$Mg+AlB_2+12B=AlMgB_{14}$	3 hours at 1050 °C
5	$MgB_2+Al+12B=AlMgB_{14}$	3 hours at 1050 °C
6	$AlB_2+MgB_2+10B=AlMgB_{14}$	3 hours at 1050 °C

### 3.4 Characterization of ReB<sub>2</sub>, OsB<sub>2</sub> and AlMgB<sub>14</sub>

#### 3.4.1 XRD

To ReB<sub>2</sub>, OsB<sub>2</sub> and AlMgB<sub>14</sub>, a small sample was removed for phase analysis by X-ray diffraction (XRD) at every certain time. A Rigaku D/MAX X-Ray Diffractometer (Cu K $\alpha$  radiation,  $\lambda=1.54056$  Å, Rigaku, Tokyo, Japan) was used to record X-ray diffraction patterns of the powder from 10 to 80 degrees, with a scan speed of 2 seconds per step and a step size of 0.01°. All the diffraction patterns are identified by JADE software (Materials Data Inc., Livermore, CA, USA). In the synthesis of osmium diboride, XRD was done with high resolution (0.002 degree/step) for the 25-hour-milled sample. The XRD data was used for Rietveld refinement.

#### 3.4.2 Microscopies

The morphology and grain size of the powders were examined using a Scanning Electron Microscope (Zeiss ULTRA-55 FEG SEM, Zeiss, Oberkochen, Germany) equipped with a field emission gun operating between 10-20 kV. In the synthesis of OsB<sub>2</sub>, Energy-dispersive X-ray spectroscopy (EDX) was applied together with SEM to identify the elements exist in the osmium and boron mixture powder. A Transmission Electron Microscope (FEI Technai F30 TEM, FEI, Amsterdam, Netherlands) was used to get finer resolution images of the synthesized particles as well as to produce an area map distribution of Re, B, and W elements in the material. In the

synthesis of OsB<sub>2</sub>, TEM was also used to perform electron diffraction. The accelerating voltage of the TEM was 300kV.

### 3.4.3 SIMS

Secondary ion mass spectrometry was used to detect impurity elements present in the mixture powder. Adept 1010 Dynamic SIMS System (Physical Electronics USA, ULVAC-PHI, Kanagawa, Japan) has been applied to collect mass spectra for the samples. Cs primary beam of 3kV and 25nA or 50nA was rastered over area 1000×1000μm. Both negative and positive secondary ions were collected. An auxiliary e-gun was used for charge neutralization.

### 3.4.4 Micro-Raman Spectroscopy

Raman spectroscopy is a spectroscopic technique used to study vibrational, rotational, and other low-frequency modes in a system. [68] A Renishaw InVia Raman spectrometer was used to study the vibrational spectra of ReB<sub>2</sub> powders. The Raman spectrometer system is comprised of two lasers (532nm and 785nm) to excite the sample, a single spectrograph fitted with holographic notch filters and a Leica optical microscope (Leica, Wetzlar, Germany) rigidly mounted and optically coupled to the spectrometer. The generated laser power was 25mW. In a Raman spectra collection, the light of a laser is focused on the sample. The spectrum of collected scattered lights is analyzed by a spectrometer and a charge-coupled device (CCD) detector. Before collecting spectra of ReB<sub>2</sub>, the spectrometer was calibrated with a Si standard using a Si

band position at  $520.3\text{cm}^{-1}$ . The average collection time for a single spectrum was 300s. Five measurements were performed from different locations of the powder in order to obtain the repeatable data. The  $50\times$  objective was used for illumination of the spot of  $3\text{-}4\mu\text{m}$  in diameter. Renishaw wire 2.0 software was used to produce two dimensional maps.

## CHAPTER 4: RESULTS AND DISCUSSIONS

### 4.1 Rhenium Diboride

#### 4.1.1 XRD

The synthesis of the desired  $\text{ReB}_2$  phase out of elemental Re and B was monitored by powder X-ray diffraction (XRD). The XRD patterns of metallic Re and B amorphous powders used for mechanochemical synthesis of  $\text{ReB}_2$  are shown in Figure 15(a) and (b). Figure 15 (c) shows the X-ray diffraction patterns of  $\text{ReB}_2$  powders after different milling times. The quantity of  $\text{ReB}_2$  increased with increased milling time. After 5, 10, 15 or even 20h of milling significant amounts of Re metal were still present. After 30 hours of milling a small amount of Re was still evident with the  $\text{ReB}_2$  formed. After 50h of ball milling no Re was detected by XRD. The peaks of (002), (100) and (103)  $\text{ReB}_2$  planes are sharper and have an increased intensity after 50h in comparison with 30h of milling, which indicates the presence of a more crystalline product. The WC phase was also present due to degradation of the milling media and vial upon contact with the abrasive product. Table 5 lists the lattice parameters of the synthesized  $\text{ReB}_2$  after mechanical alloying for 30, 50 and 80h, and lattice parameters of  $\text{ReB}_2$  reported in the literature (PDF card # 01-073-1392) are also given for comparison [22]. As one can see from the Table 5, the measured lattice parameters match closely to the reported values. It is also noted that the lattice parameters slightly decrease with increase in mechanical alloying time, while the  $c/a$  ratio increases with longer mechanical alloying time approaching the reported value.

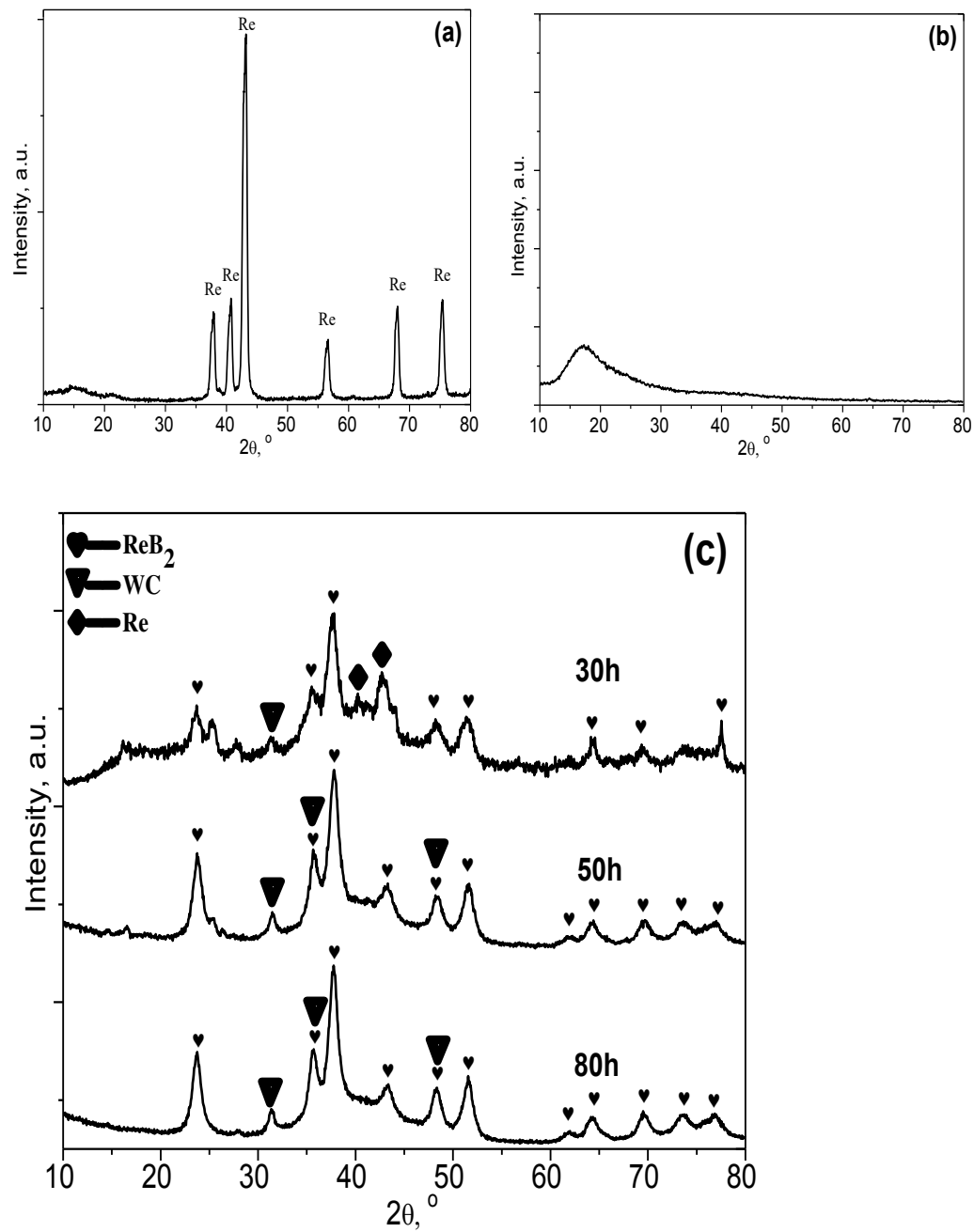


Figure 15: (a) X-ray diffraction patterns of Re powder, (b) B powder and (c) ReB<sub>2</sub> mechanically alloyed powders after 30, 50, and 80 hours of milling. The observed broad peak at  $\sim 18^\circ$   $2\theta$  in (b) is a common peak seen for amorphous materials.



Table 5: Lattice parameters of the synthesized ReB<sub>2</sub> after mechanical alloying for 30, 50 and 80 hours.

Mechanical alloying time (hour)	a (Å)	c (Å)	c/a ratio
30	2.9176	7.5023	2.5714
50	2.9057	7.4867	2.5766
80	2.9018	7.4867	2.5800
PDF#01-073-1392 [21]	2.9000	7.4780	2.5786

#### 4.1.2 Microscopies

Figure 16 presents an SEM micrograph of the ReB<sub>2</sub> powders after 80h of milling. It can be seen that a wide particle size distribution is observed. The size of the largest agglomerates is about 1 μm. Along with morphology study of agglomerates by SEM, high resolution characterization of selected particles was performed using TEM. A typical particle of mechanochemically synthesized ReB<sub>2</sub> and its electron diffraction are shown in Figure 17. The particle size is about 60nm wide and 150nm long. It consists of a number of crystallites 5-10nm in diameter agglomerated together. The selected area electron diffraction pattern of the particle shows clearly defined diffraction spots, indicating that the particle is crystalline in nature. The maps of the distribution of Re, B, and W (Figure 18) show that the distribution of B is not homogeneous and a high concentration of boron can be seen in a location at one side of the particle under study. Tungsten was also located on the opposite side of the particle, thus confirming the XRD data of contamination of the ReB<sub>2</sub> by the material used to make the vial and milling media.

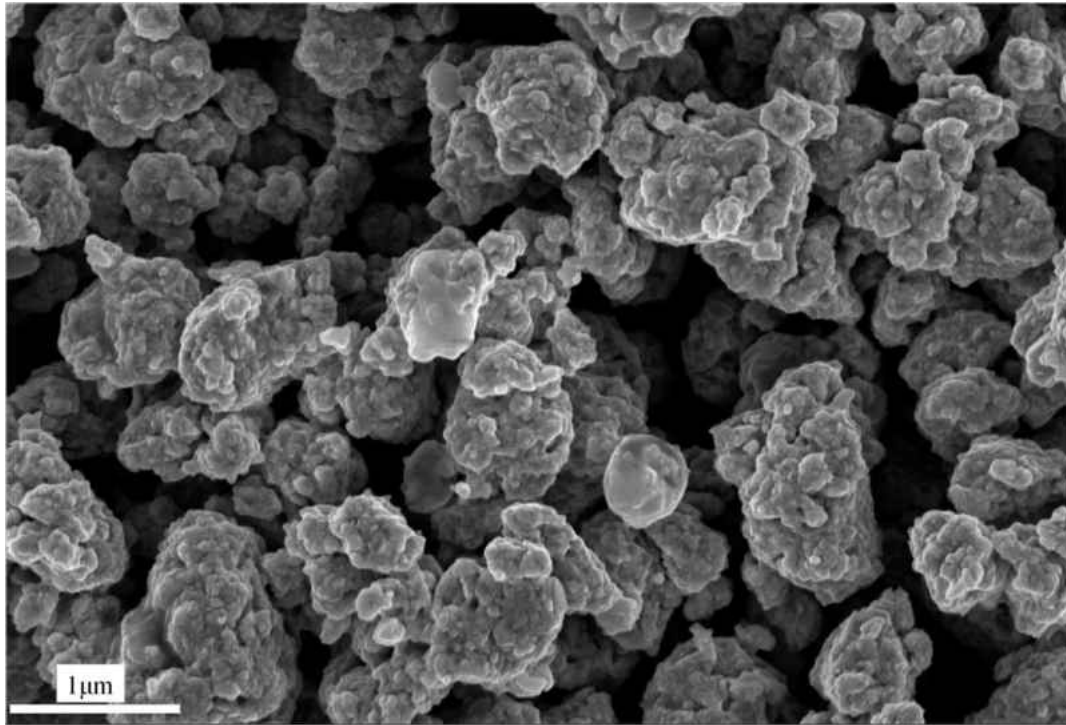


Figure 16: SEM micrograph of ReB<sub>2</sub> powders after ball milling for 80 hours.

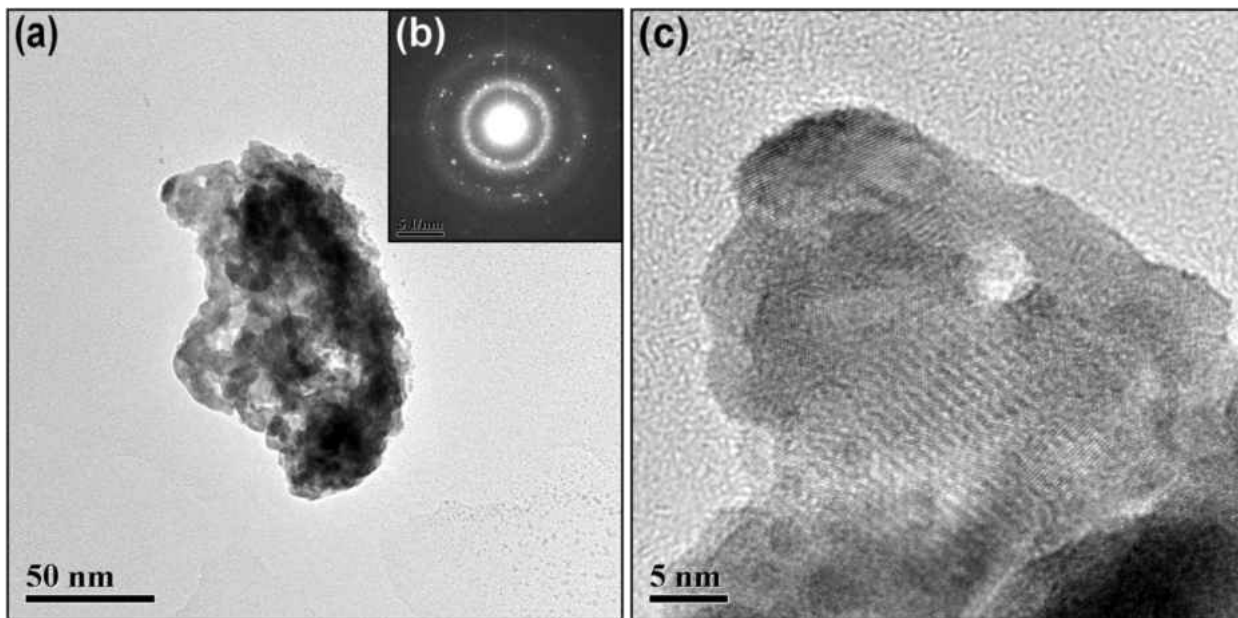


Figure 17: (a) TEM micrograph of a particle of ReB<sub>2</sub> powder after 80 hours of milling, (b) Electron diffraction of ReB<sub>2</sub> particle, (c) TEM micrograph of ReB<sub>2</sub> lattice fringes.

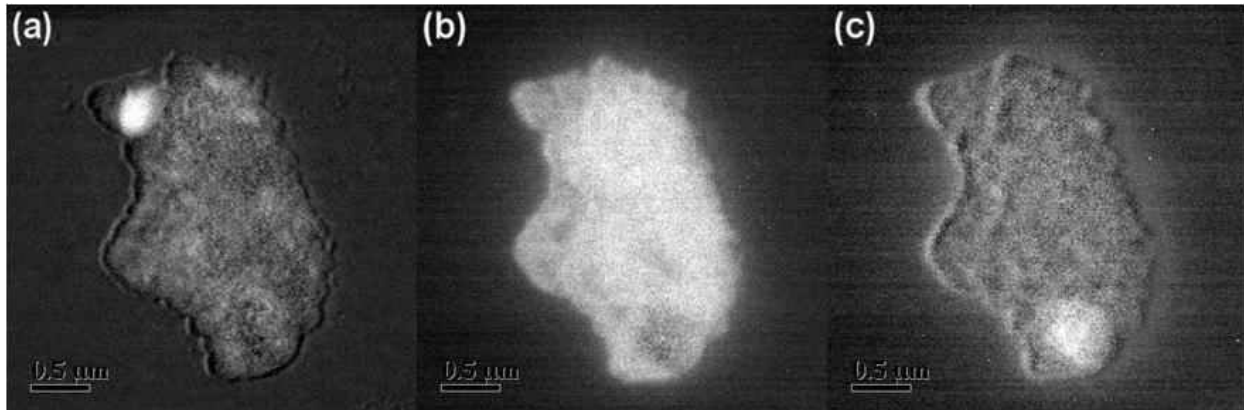


Figure 18: Distribution maps of (a) Boron, (b) Rhenium, (c) Tungsten in  $\text{ReB}_2$  particle obtained

#### 4.1.3 SIMS

The presence of a number of impurities was also confirmed by SIMS. It can be seen from Figure 19(a), that oxygen was detected in the mixture after milling for 0.5h since the  $^{16}\text{O}$  peak was present along with other oxygen containing peaks such as  $\text{O+B}$ ,  $\text{O}_2$ , and  $\text{BO}_2$ . The intensity of the  $^{16}\text{O}$  peak increased relative to the intensity of  $^{10,11}\text{B}$  peak as milling time was increased indicating the further O contamination of the powders. The relative intensity of O, BO and  $\text{BO}_2$  peaks over the  $^{10,11}\text{B}$  peak is shown in Table 6 and one can see that the oxygen content increased as milling time increased from 0.5h to 40h reaching a saturation point since the oxygen content did not increase significantly from 40h to 80h of milling. The  $\text{Re+O}$  peak intensity was also compared to the  $\text{Re+B}$  peak intensity for all three milling times. The intensity ratios of these peaks are presented in Table 6 and it is consistent with the increase in oxygen content after milling. Prominent among the other impurities were C, F, and Cl. While it was detected that the carbon content decreased with increased milling time, the F and Cl content increased upon milling for 40h, but decreased after 80h milling. This indicates that the impurities were not

distributed homogeneously in the powder, and the probes that were taken for analysis were not homogeneous; otherwise we should see the increase of the impurities content as time of milling increased.

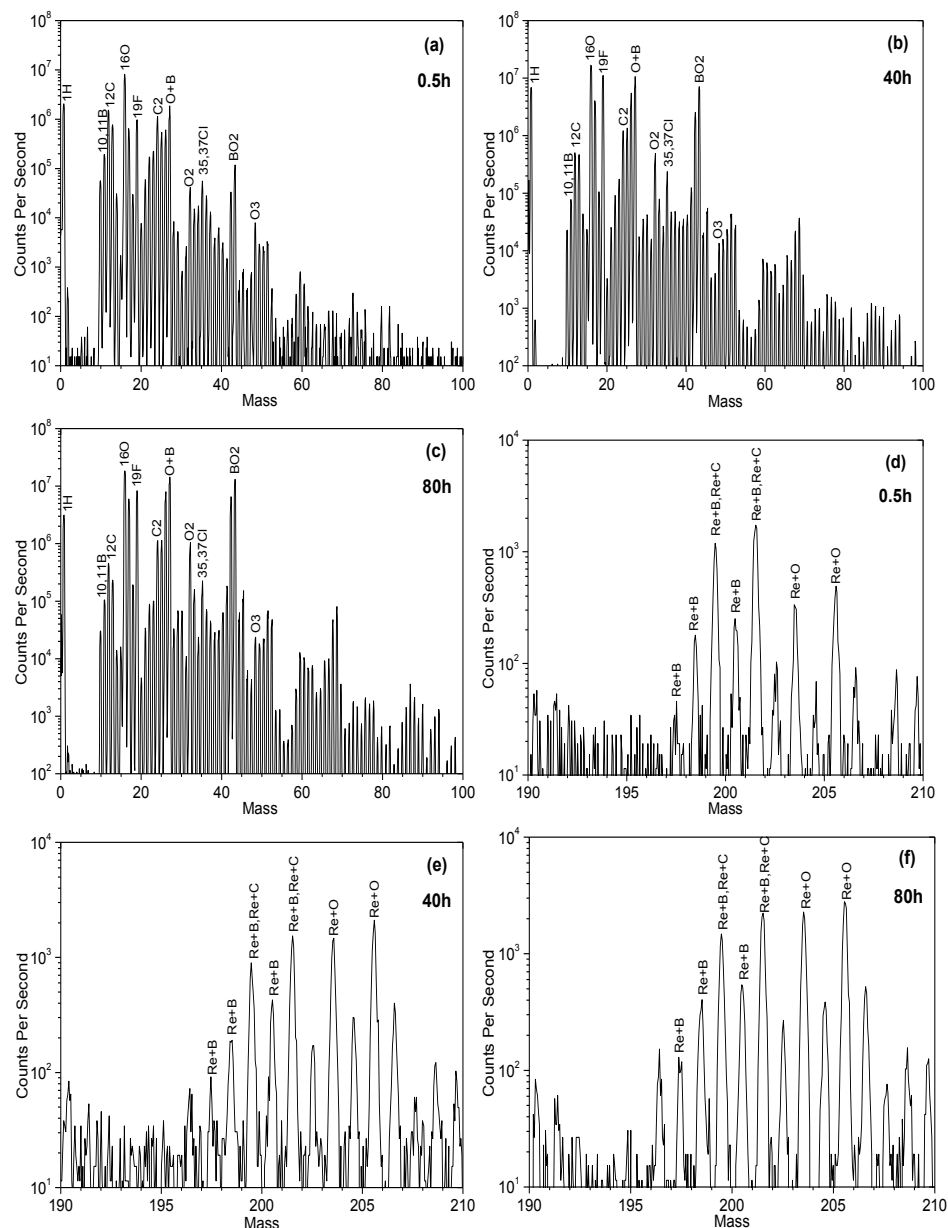


Figure 19: Negative secondary ion mass spectrometry of  $\text{ReB}_2$  powders after 0.5h (a, d); 40h (b, e); and 80h (c, f) milling time.

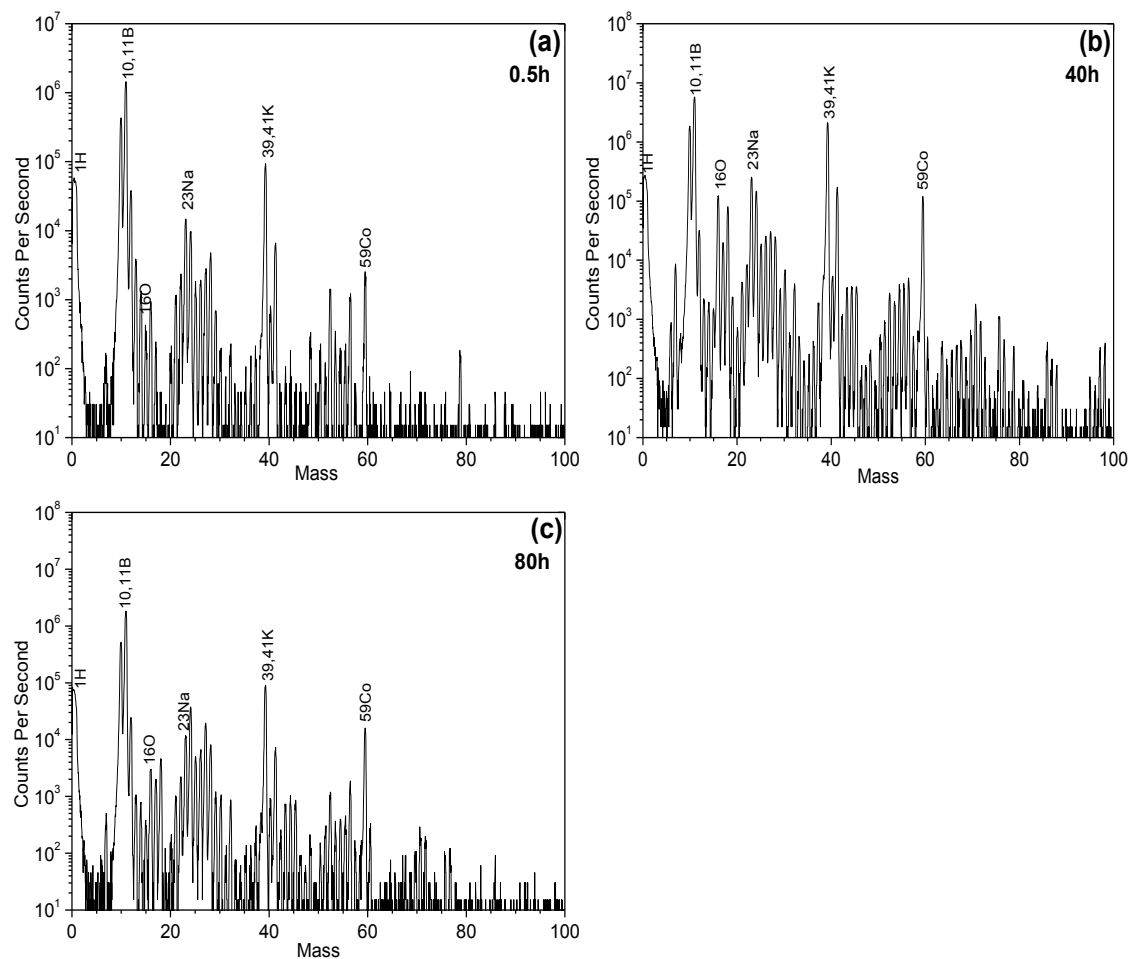


Figure 20: Positive second ion mass spectrometry of  $\text{ReB}_2$  powders after 0.5h (a); 40h (b); and 80h (c) milling time.

Interestingly, hydrogen was detected in the powder after 30 minutes as well as after prolonged milling. The relative intensity of the H peak was the lowest after 30 minutes of milling and increased after longer milling. This could indicate the presence of water in the batch during milling. Positive secondary ions are more sensitive to detect metallic contaminations and they were used to detect metallic impurities present in Figure 20. Both Na and K were detected and their quantity increased upon increase in the milling time. However, their quantity was small after 80h of milling in comparison with 40h of milling time, which could be explained by the

non-homogeneous distribution of the elements in the batch. Co was also detected, as WC alloy contains Co as a soft binder in WC-Co cement composite.

Table 6: Intensity ratio of impurities to boron SIMS peaks.

Intensity Ratio		Time, hour		
		0.5	40	80
Negative secondary ions	$\text{BO}/^{10,11}\text{B}$	9.6900	138.89	136.99
	$\text{BO}_2/^{10,11}\text{B}$	0.9414	91.743	125.00
	$\text{Re+O}/\text{Re+B}$	1.9547	4.9285	5.1546
	$^{12}\text{C}/^{10,11}\text{B}$	7.9069	6.5309	4.3346
	$^{19}\text{F}/^{10,11}\text{B}$	5.0478	143.95	78.667
	$^{35,37}\text{Cl}/^{10,11}\text{B}$	0.2895	3.0687	2.1380
	$^1\text{H}/^{10,11}\text{B}$	10.666	89.451	29.868
Positive secondary ions	$^{16}\text{O}/^{10,11}\text{B}$	0.0007	0.0214	0.0016
	$^{39,41}\text{K}/^{10,11}\text{B}$	0.0647	0.3678	0.0496
	$^{59}\text{Co}/^{10,11}\text{B}$	0.0018	0.0208	0.0087
	$^{23}\text{Na}/^{10,11}\text{B}$	0.0102	0.0441	0.0065

#### 4.1.4 Raman spectroscopy

Raman spectra of  $\text{ReB}_2$  powders were acquired using two 532nm and 785nm lasers (Figure 21). Factor group analysis of  $\text{ReB}_2$  hexagonal structure results in 2  $E_{1g}$  and 2  $E_{2g}$  Raman active phonon modes, where  $E_{1g}$  and  $E_{2g}$  modes are reported as B-B pair atom vibrations in a-b plane of the unit cell as an “out-of-phase” vibrations with a calculated phonon energy of 85.2

MeV for E1g mode and 90.4 MeV for E2g mode 4. In the spectrum collected with IR frequencies, two bands are detected: one at  $190\text{ cm}^{-1}$  and another at  $\sim 786\text{ cm}^{-1}$ . In the spectrum collected using visible laser, two peaks at  $\sim 228\text{ cm}^{-1}$  and  $780\text{ cm}^{-1}$  wave numbers are also detected, but in addition two  $\sim 1400\text{ cm}^{-1}$  and  $1580\text{ cm}^{-1}$  broad bands are present. These  $1400\text{ cm}^{-1}$  and  $1580\text{ cm}^{-1}$  bands indicate the presence of carbon, which is explained by contamination of the  $\text{ReB}_2$  powders by milling. Due to the current experimental set up of the notch filter in the Invia spectrometer, only bands with wave numbers higher than  $180\text{ cm}^{-1}$  could be detected.

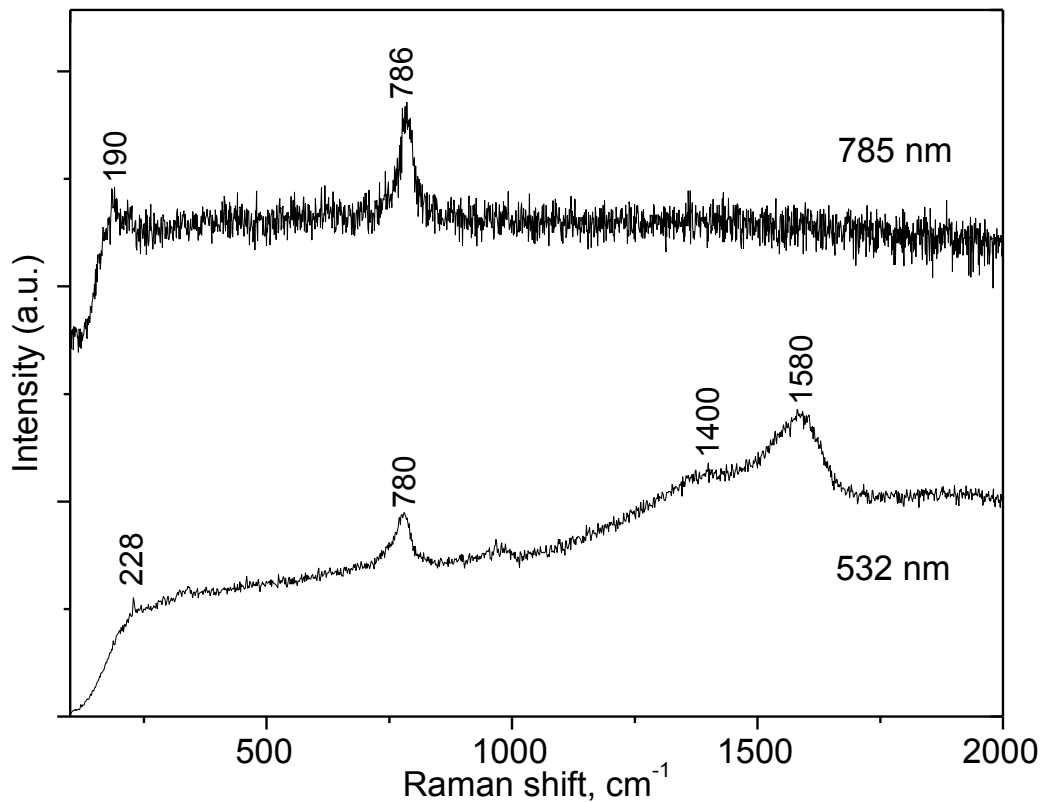


Figure 21: Raman spectra of mechanically alloyed  $\text{ReB}_2$  powders after 80 hours of ball milling.

#### 4.1.5 Reaction of powder ReB<sub>2</sub> with O<sub>2</sub> and H<sub>2</sub>O

Upon storing ReB<sub>2</sub> powder in air, packed in the plastic bag; it was found that the powders formed hard agglomerates. The XRD pattern of the long time stored powder is shown in Figure 22. This may be due to a sequential attack by oxygen and water. Initially oxygen may react with the surface of ReB<sub>2</sub> to form Re<sub>2</sub>O<sub>7</sub> and B<sub>2</sub>O<sub>3</sub> (Eq. 7).



This reaction is thermodynamically favored with a heat of reaction of -1235.3 kJ/mol of ReB<sub>2</sub>. Not only is there a severe lattice mismatch between these oxides and the ReB<sub>2</sub> compound but they quickly react with atmospheric water to form boric acid (Eq 8, -629.3 kJ/mol) and perrhenic acid (Eq. 9, -55.812 kJ/mol).



The net reaction (Eq. 10) is enthalpically favored by -7.592 kJ/mol. [69], [70]



These acids are hygroscopic and create a liquid layer that allows further degradation of the bulk material. In fact, storage of this material in air while in contact with nylon 6,6 results in holes in the nylon due to acidic degradation. Equations 7 through 10 suggest that applications of ReB<sub>2</sub> will require exclusion of oxygen or water vapors since the reaction sequence cannot proceed without both. High surface area powders are more susceptible than solid billets.



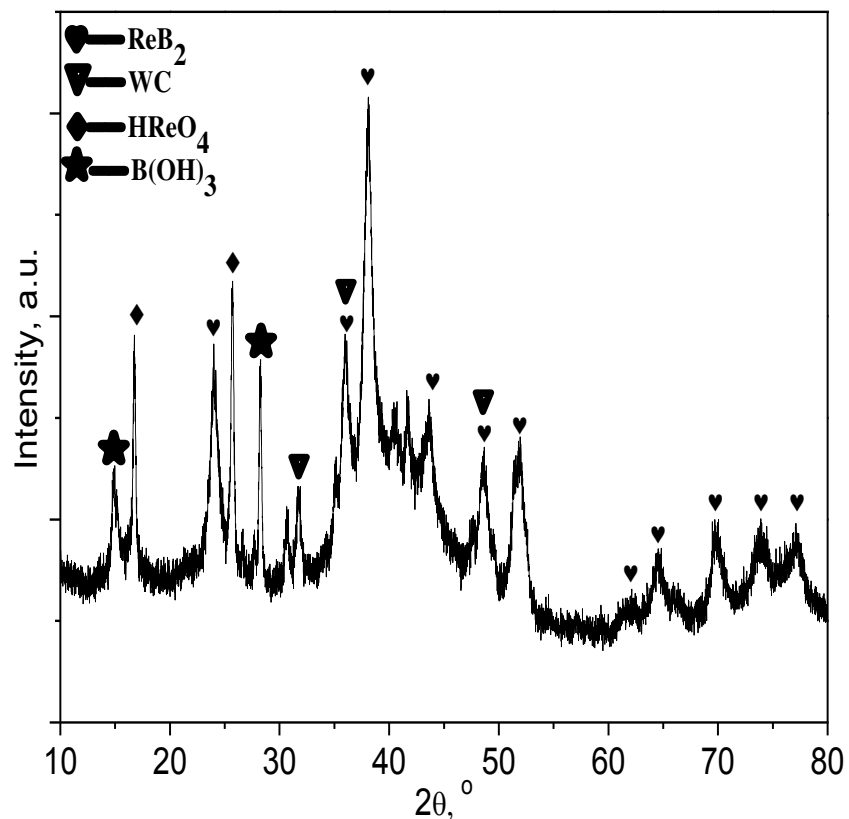


Figure 22: X-ray diffraction patterns of  $\text{ReB}_2$  powder after 1 year storage in the plastic bag without any protective atmosphere.

## 4.2 Osmium Diboride

### 4.2.1 XRD

In the earlier experiment, Os and B mixture was milled for 33 hours. It was found that a group of unknown XRD patterns existed apart from the identified  $\text{OsB}$ . It does not match with the given orthorhombic  $\text{OsB}_2$  pattern (PDF# 017-0370) but matches with the  $\text{ReB}_2$  pattern (PDF# 00-011-0581) very well. It can be seen that Re and Os are adjacent in periodic table and their

atomic structures are very similar. Also, in the previous work  $\text{ReB}_2$  was mechanochemically synthesized by the same approach. It is possible that osmium diboride was formed, which has the same hexagonal structure with  $\text{ReB}_2$ . Here we assume this phase is hexagonal  $\text{OsB}_2$ .

A new set of experiments were repeated. XRD patterns of powder mixture with different milling time were shown in Figure 23. It was found that the experiment was repeatable.  $\text{OsB}$  formed after the first 2 hours of milling, and very weak intensity of  $\text{OsB}_2$  was observed. After 6 hours of milling, the intensity of  $\text{Os}$  decreased a lot and the major phase was  $\text{OsB}$ ,  $\text{OsB}_2$  also show stronger intensity. When the mixture was milled by 14 hours, there was still some  $\text{Os}$  left, but it has a very weak intensity, while the  $\text{OsB}_2$  became the major phase. After that, it looks the intensity of  $\text{OsB}$  increased. However, that was because the XRD pattern of  $\text{OsB}$  and  $\text{WC}$  are almost overlapped. With the milling time increasing, more  $\text{WC}$  debris was chipped off from vial or balls. Besides, samples were taken every 2 hours made the ball to powder mass ratio increase, which lead to stronger collision between balls and vial, and created more  $\text{WC}$  debris. It can be seen that the 14 hour milled sample has high  $\text{OsB}_2$  concentration but less  $\text{WC}$  contamination.

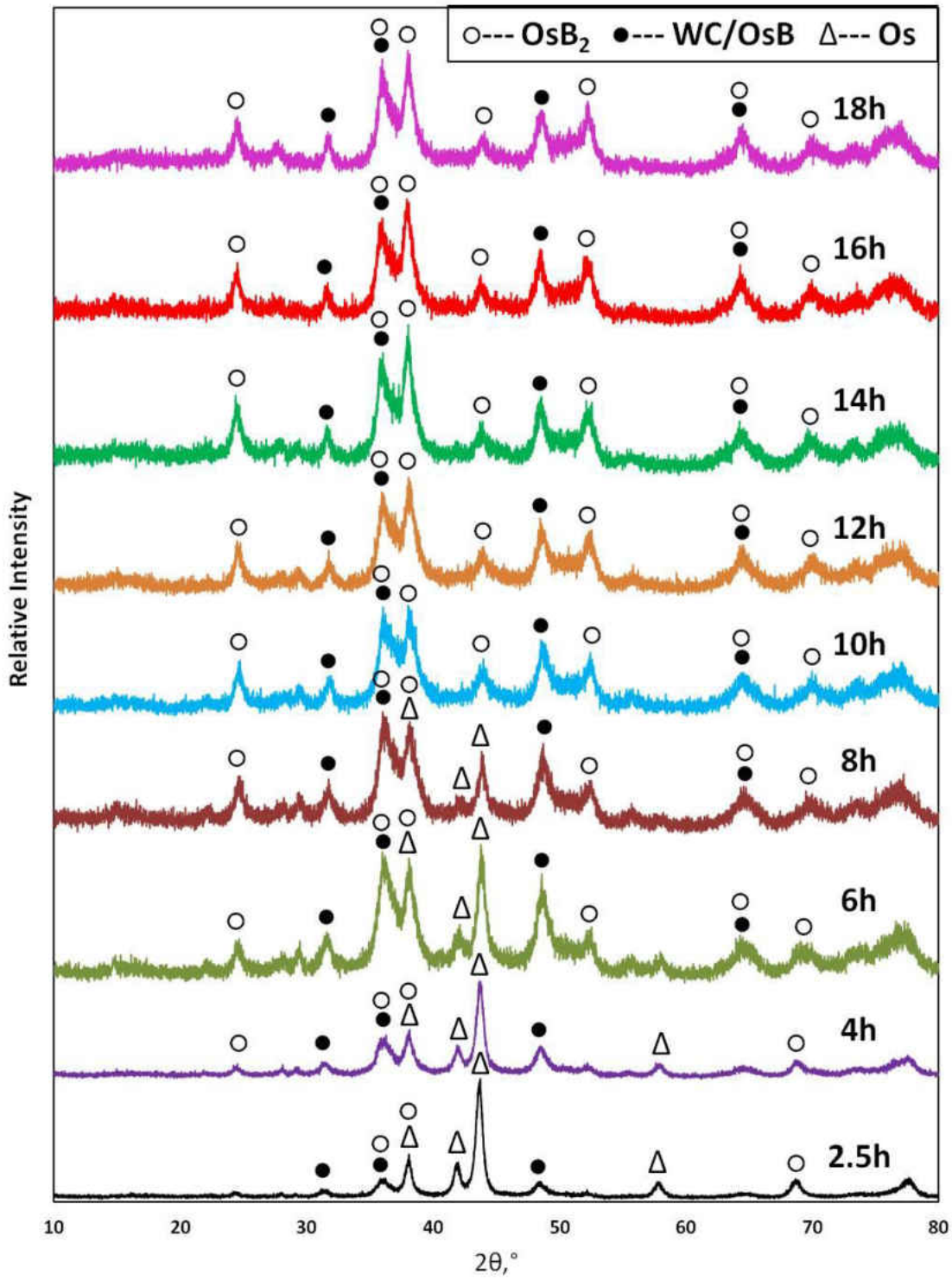


Figure 23: XRD patterns of Os and B mixture at different milling time.

High resolution XRD was done on the 25-hour-milled sample. The XRD pattern was Rietveld refined and analyzed by GSAS+EXPGUI. [71,72] Figure 24 shows the refined XRD pattern. Lattice parameters were obtained from the Rietveld refined pattern. Table 7 listed the lattice parameters of the mechanochemically synthesized  $\text{OsB}_2$ ,  $\text{ReB}_2$  and the reported  $\text{OsB}_2$  parameters (by theoretical calculation) [9]. It shows the lattice parameters of our synthesized  $\text{OsB}_2$  are very close to that of the  $\text{ReB}_2$ , and also close to the simulated results. The unit cell of hexagonal and orthorhombic  $\text{OsB}_2$  were shown in Figure 25.

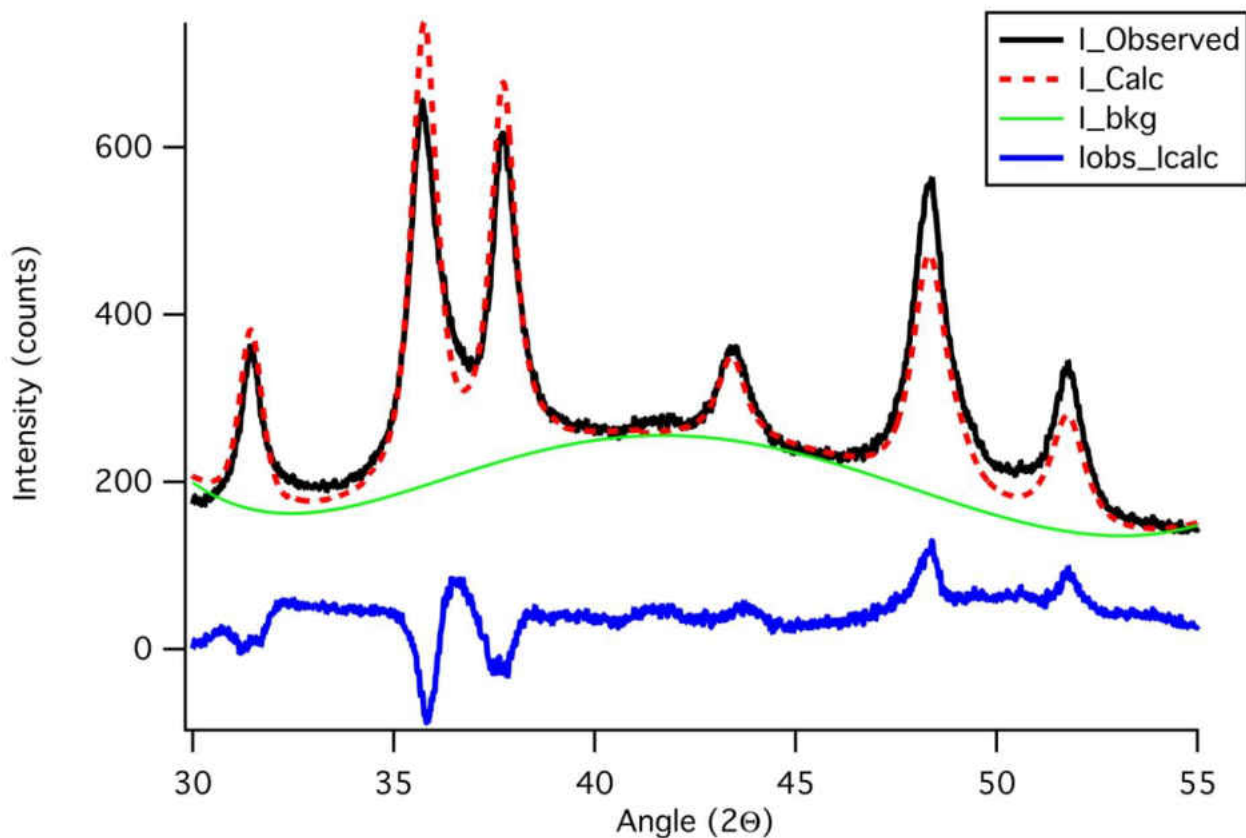


Figure 24: Rietveld refinement XRD pattern of Os and B mixture milled for 25 hours.

Table 7: Lattice parameters of the mechanochemically synthesized OsB<sub>2</sub>, simulated OsB<sub>2</sub> and ReB<sub>2</sub>.

Lattice parameter data source	a (Å)	c (Å)	c/a ratio
synthesized	2.905	7.450	2.565
ReB <sub>2</sub> PDF#01-073-1392 [21]	2.900	7.478	2.579
Theoretical calculation (GGA)	2.941	7.338	2.495

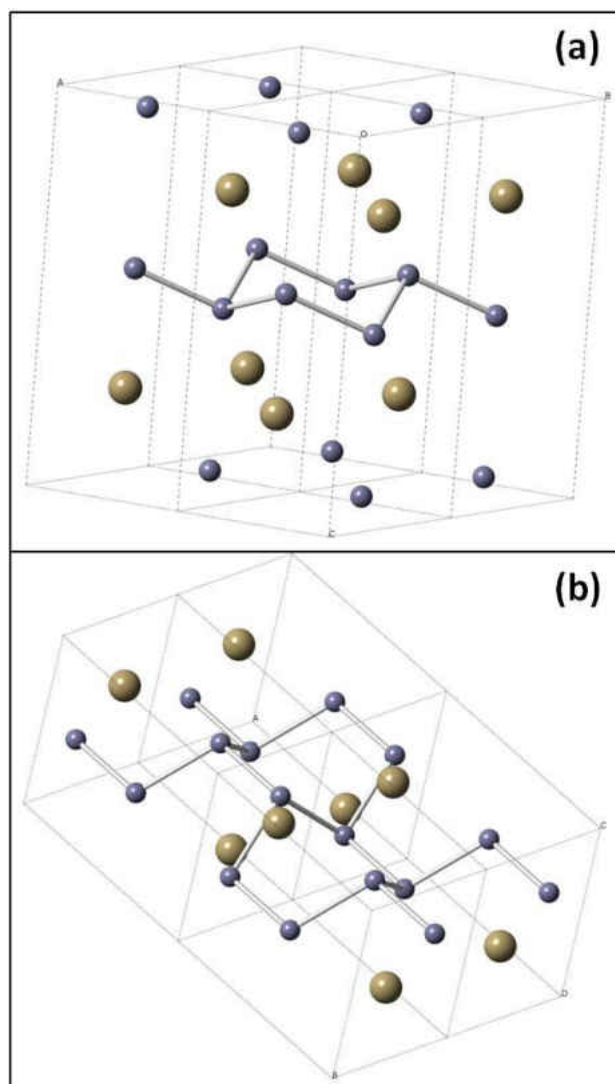


Figure 25: Unit cells of hexagonal (a) and orthorhombic (b) OsB<sub>2</sub>.

#### 4.2.2 SEM and EDX

Figure 26 presents an SEM micrograph of the  $\text{OsB}_2$  powders after 14h of milling. A wide particle size distribution is observed. Most of the particles are smaller than  $10\ \mu\text{m}$ , while the largest agglomerate is about  $30\ \mu\text{m}$ . Since the XRD pattern of the assumed hexagonal  $\text{OsB}_2$  matched with that of the  $\text{ReB}_2$ , EDX was applied in order to make sure that no contamination of Re in the mixture. The EDX result was shown in Figure 27. It can be seen that no Re detected. W is from the grinding media WC; C is from both WC and conductive carbon tape; and O existed due to the oxidization of B.

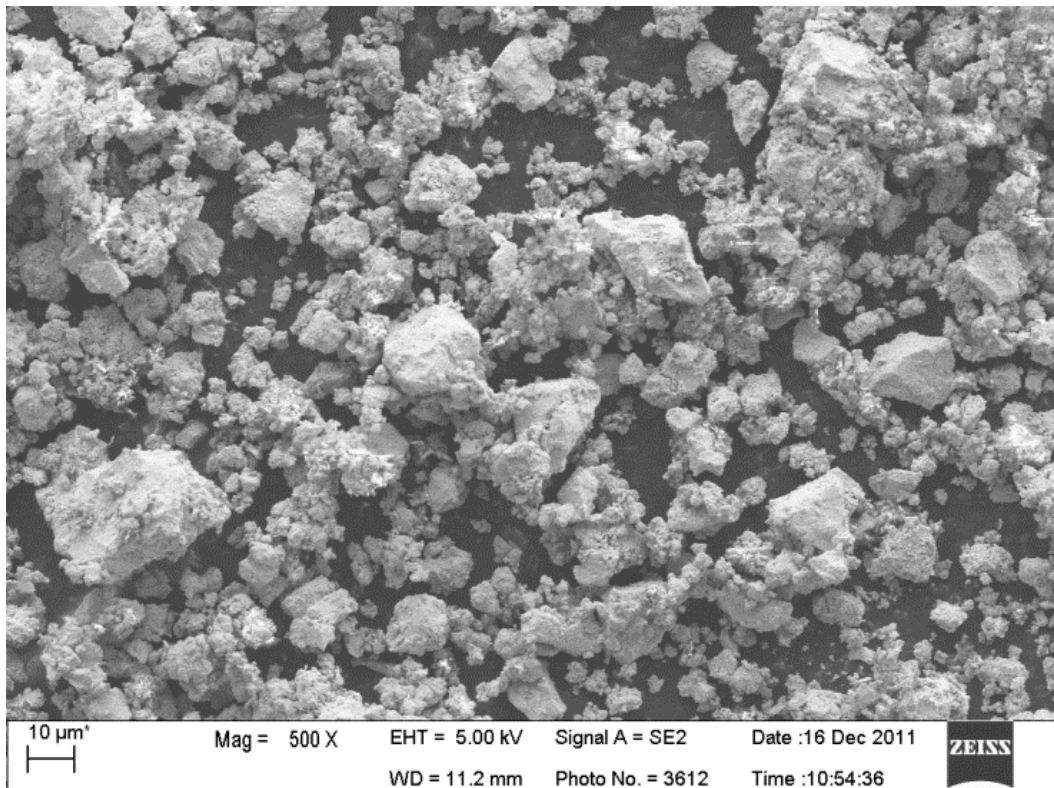


Figure 26: SEM of Os and B mixture milled for 14 hours.

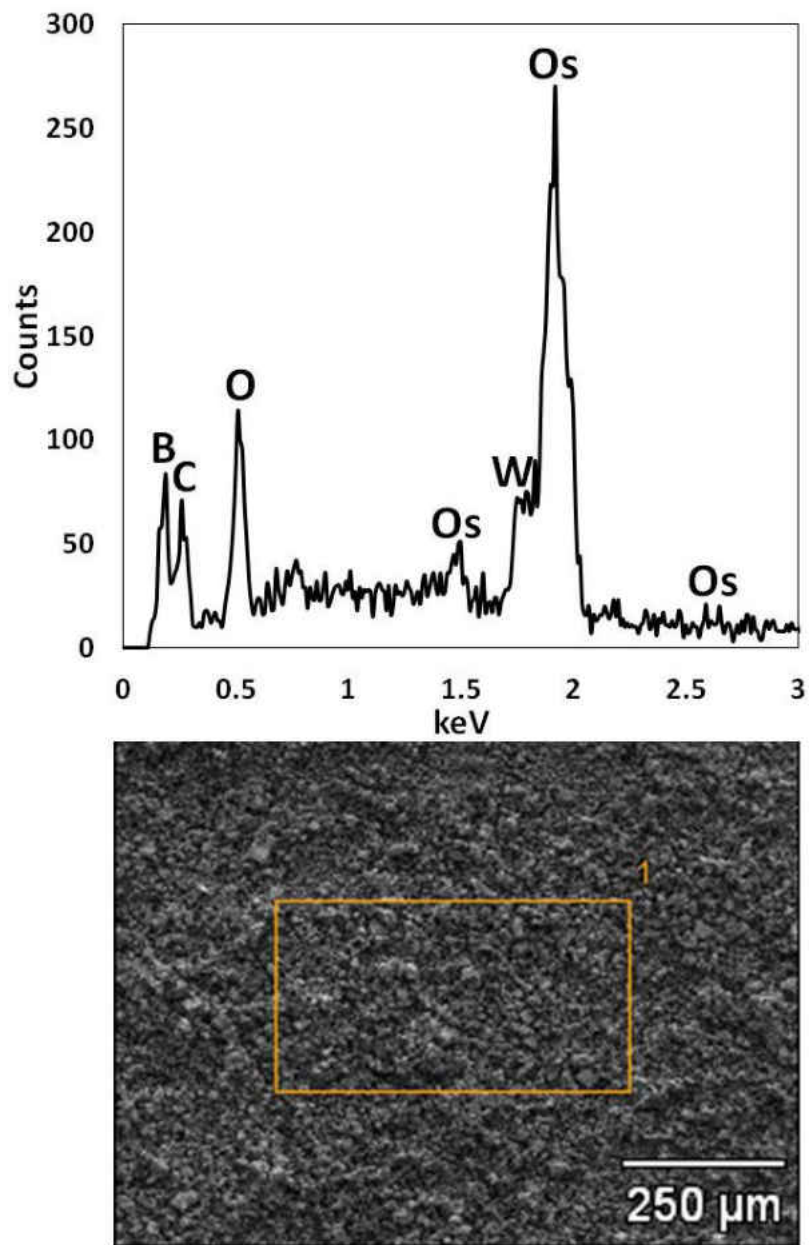


Figure 27: EDX of the Os and B mixture milled for 14 hours.

#### 4.2.3 TEM

Along with morphology study of agglomerates by SEM, high resolution characterization of selected particles was performed using TEM. A typical particle of mechanochemically

synthesized OsB<sub>2</sub> was shown in Figure 28. The particle size is about 0.4 μm wide and 1 μm long. It consists of a number of crystallites 5-10 nm in diameter agglomerated together. The high resolution image was shown in Figure 29. The selected area electron diffraction pattern of the particle shows clearly defined diffraction spots in Figure 30. In those diffraction spots, spots B, C, D and E were the strongest. The distance of BE and CD were measured to be 4.8237 Å. Apply the Bragg's law,

$$n\lambda = 2d \sin \theta \quad (11)$$

let wave length  $\lambda$  be 1.5418 Å for Cu K $\alpha$ ;  $d=1/2BE=1/2CD=2.4119$  Å; when  $n=1$ , the corresponding characteristic peak position  $2\theta$  was found to be about 37.25°, which is very close to the XRD result  $2\theta=37.75^\circ$  for the strongest peak. This confirms the particle observed is OsB<sub>2</sub>.

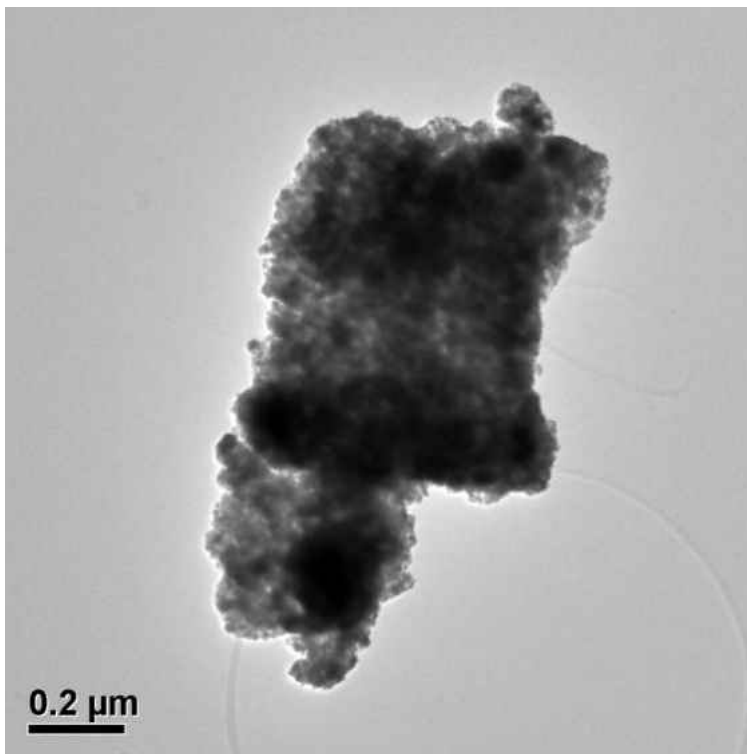


Figure 28: Transmission electron micrograph of a particle of OsB<sub>2</sub> powder.



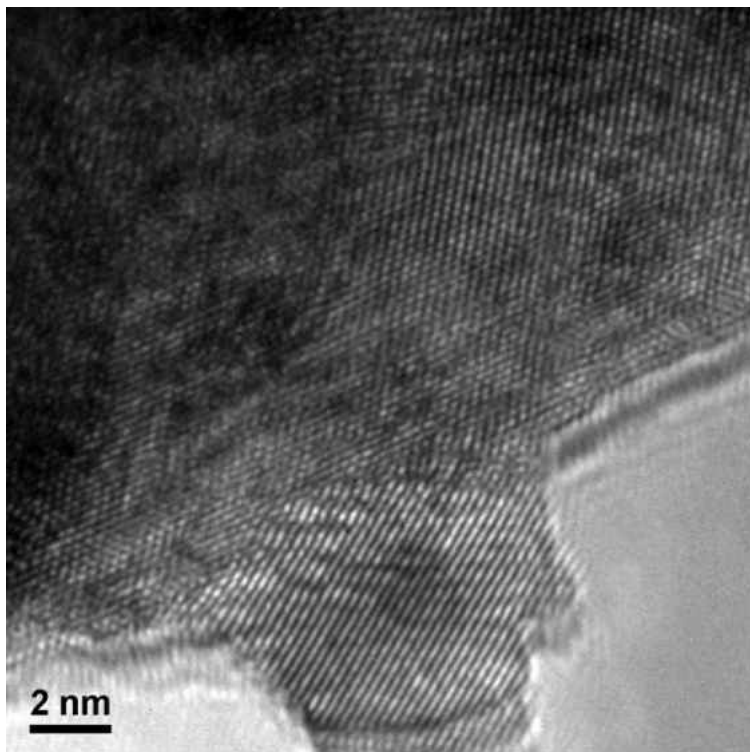


Figure 29: Transmission electron micrograph of OsB<sub>2</sub> lattice fringes.

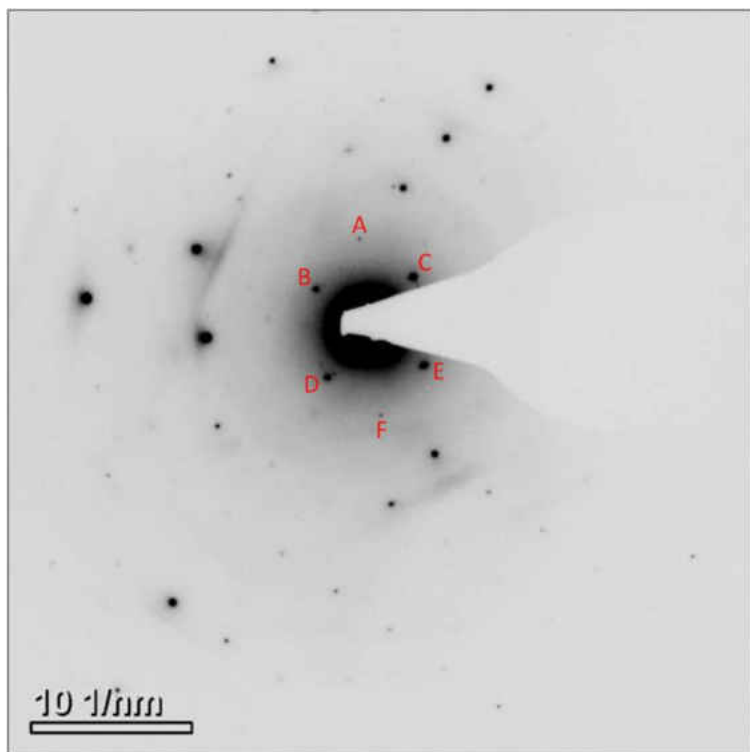


Figure 30: Electron diffraction pattern of OsB<sub>2</sub> particle.

Figure 31 shows the XRD pattern of the sample after annealing. It can be seen that the crystallinity of each phase increased, but the hexagonal phase did not transform to orthorhombic phase, even though the hexagonal phase was predicted as metastable phase.

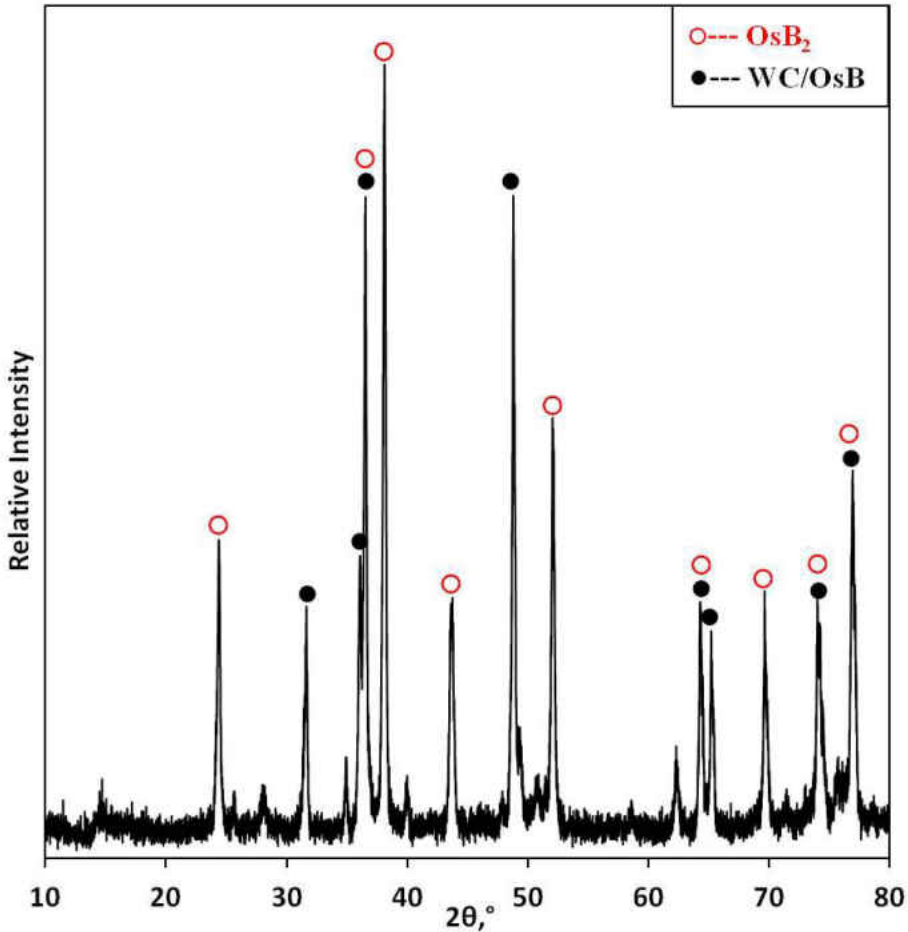


Figure 31: XRD pattern of annealed Os and B mixture.

An interesting phenomenon was observed when the author was washing the vials after milling. A lot of small bubbles came off from the inner wall of the vial. It is possible that the gas is hydrogen, which is formed by the reaction



It shows that boron powder became very reactive after milling, because boron does not react with water normally. Such reactive boron can also react with oxygen and water in the air.

The phase transition of  $\text{OsB}_2$  from orthorhombic to hexagonal structure has not been experimentally found even if the pressure reached 32 GPa [9]. This is because the orthorhombic structure is already the most stable structure to  $\text{OsB}_2$ . [18] Once the orthorhombic  $\text{OsB}_2$  is formed, it may be very hard to change it to hexagonal, the metastable phase. However, it is possible to reach the metastable state from the original state. Furthermore, Boldyrev reported that products produced by mechanochemical reactions may differ from those of thermochemical ones for the same reactants. [73] It is also reported that ball milling is a good way to synthesize metastable phases, amorphous alloys and nanostructure compounds. [57] Ball milling creates shear force, which can cause the deformation in crystals easier than pure pressure. That is because shear changes the symmetry of a solid or molecule. The electronic structure of bonds in solids becomes unstable after the breaking of symmetry, which makes the solid tend to have chemical reaction. [54] Maybe that is why hexagonal  $\text{OsB}_2$  can be produced by ball milling.

### 4.3 AlMgB<sub>14</sub>

#### 4.3.1 Experiment 1

The XRD patterns of milled powders were shown in Figure 32. It shows no  $\text{AlMgB}_{14}$  was synthesized merely by ball milling. The powders are turning to be amorphous with the milling time increase.

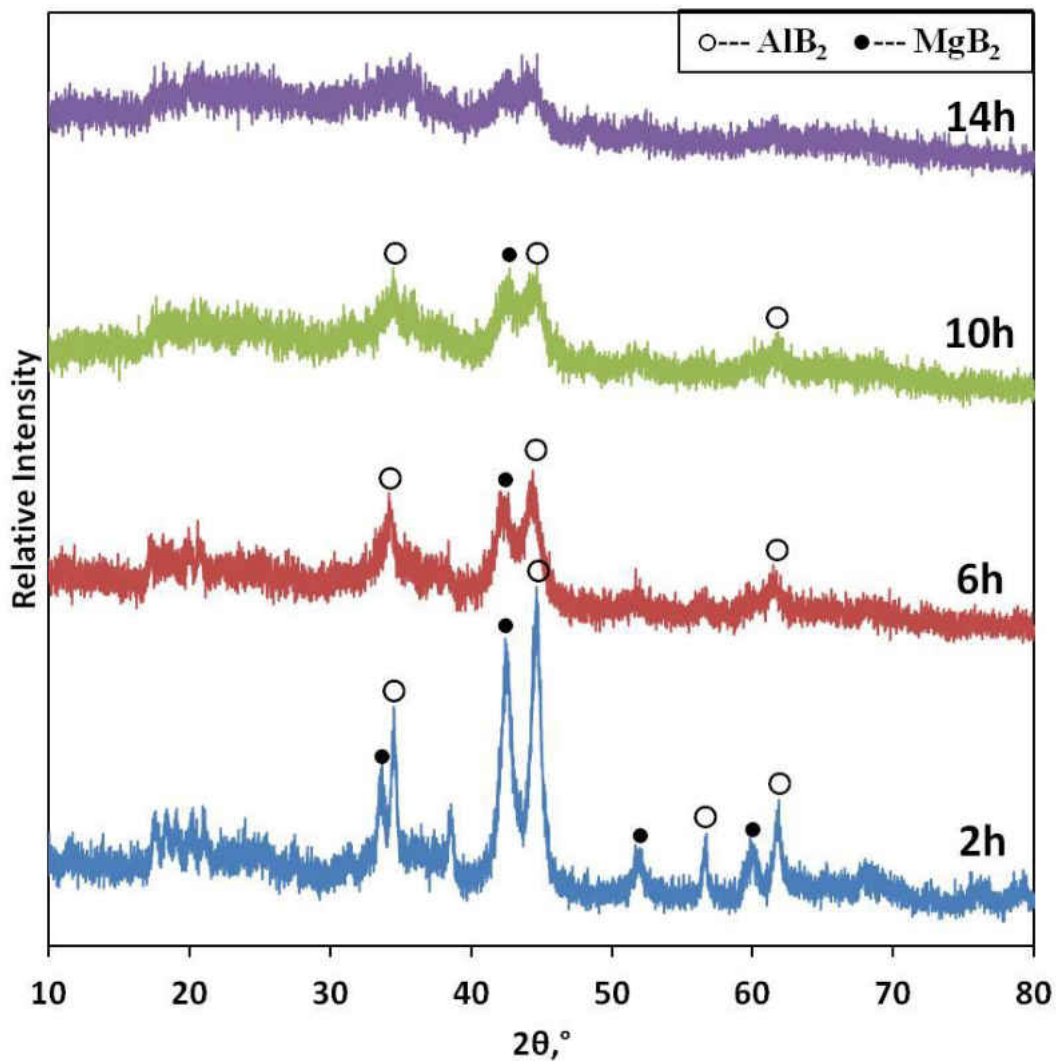


Figure 32: XRD pattern of  $\text{AlB}_2$ ,  $\text{MgB}_2$ , B mixture milled for 2h, 6h, 10h and 14h.

Figure 33 shows the displacement versus temperature curve of the sample during sintering. It can be seen that with temperature and pressure increasing sample powders were densified, which lead to the displacement of the presser. When temperature is close to 1450 °C, the displacement becomes very small. That means the powders cannot be densified any more. The XRD pattern of the spark plasma sintered sample was shown in the Figure 34. The spinel

MgAl<sub>2</sub>O<sub>4</sub> can be observed as the major phase from the pattern, and almost no AlMgB<sub>14</sub> product was formed. The oxygen contamination is due to the mixture powder was exposed to air when filling the graphite dies or serious oxidization happened during milling. The other contamination is WC, which is due to the debris chipped from milling vials and milling media.

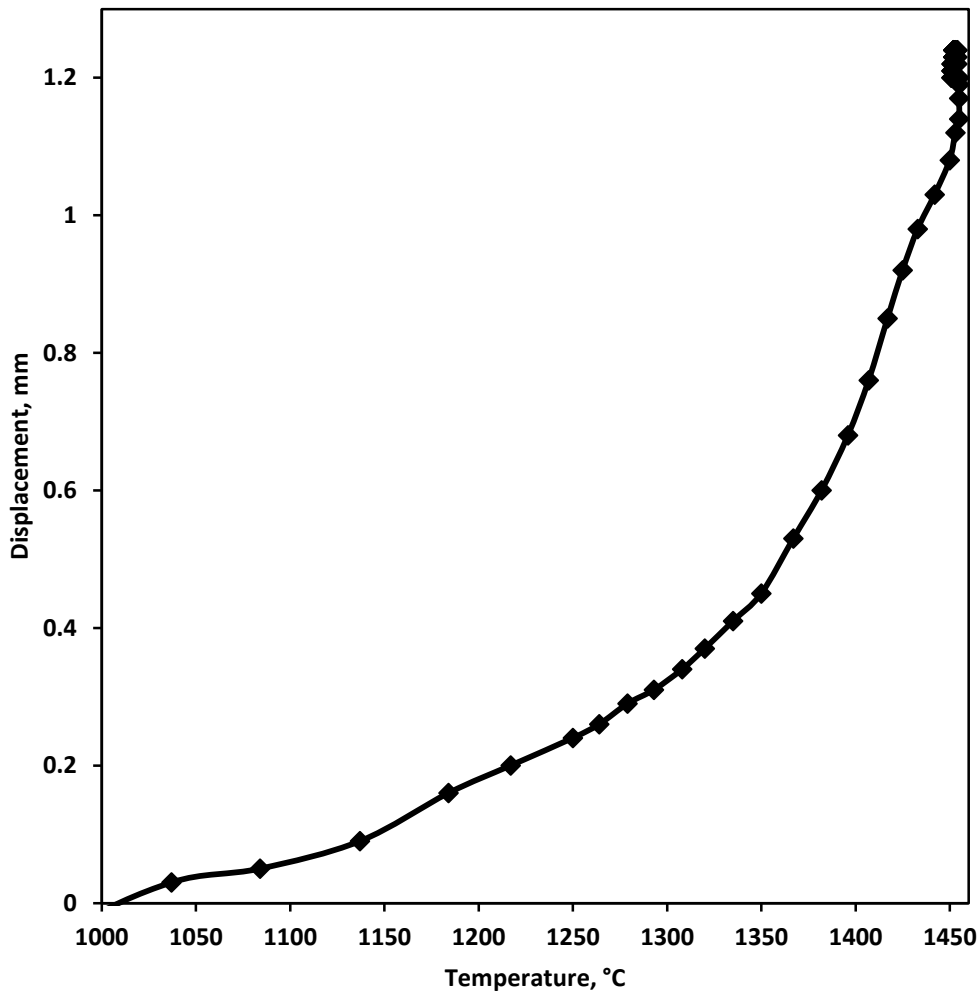


Figure 33: Heating curve of the spark plasma sintering.

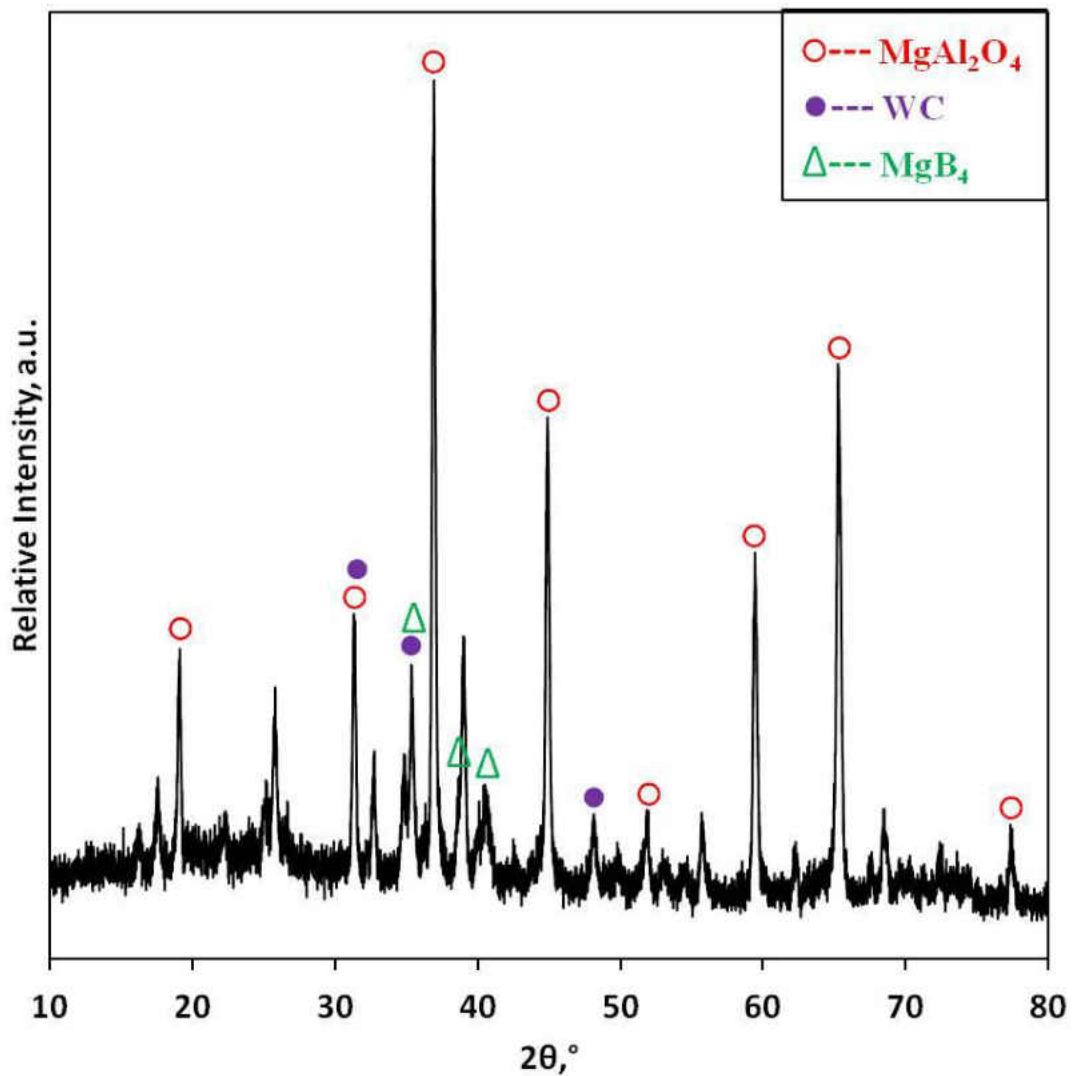


Figure 34: XRD patterns of the milled mixture powder after spark plasma sintering.

#### 4.3.2 Experiment 2

The XRD patterns of the milled powders (with ball to powder mass ratio 4:1) were shown in Figure 35. The results were very similar to that of the first experiment: no  $\text{AlMgB}_{14}$  was observed and the mixture turned to be amorphous after milling. XRD pattern of the powder

milled with ball to powder mass ratio 10:1 was shown in Figure 36. It can be seen that the intensity of the elemental materials were weaker, and strong intensity of WC can be observed. Besides, a big crack was observed on the inner wall of a vial. It shows that increasing the ball to powder mass ratio cause damage to the vial, but no significant contribution on synthesis. The sintered sample also shows no  $\text{AlMgB}_{14}$  exist, and the major phase was the spinel  $\text{MgAl}_2\text{O}_4$ . After checking all the equipments, it was found that the oxidization happened in the milling step. The vibration during milling made the cap of the vial loosed somehow and not tight enough to prevent air going into the vial. This is why the ball milling step was given up in the later experiments.

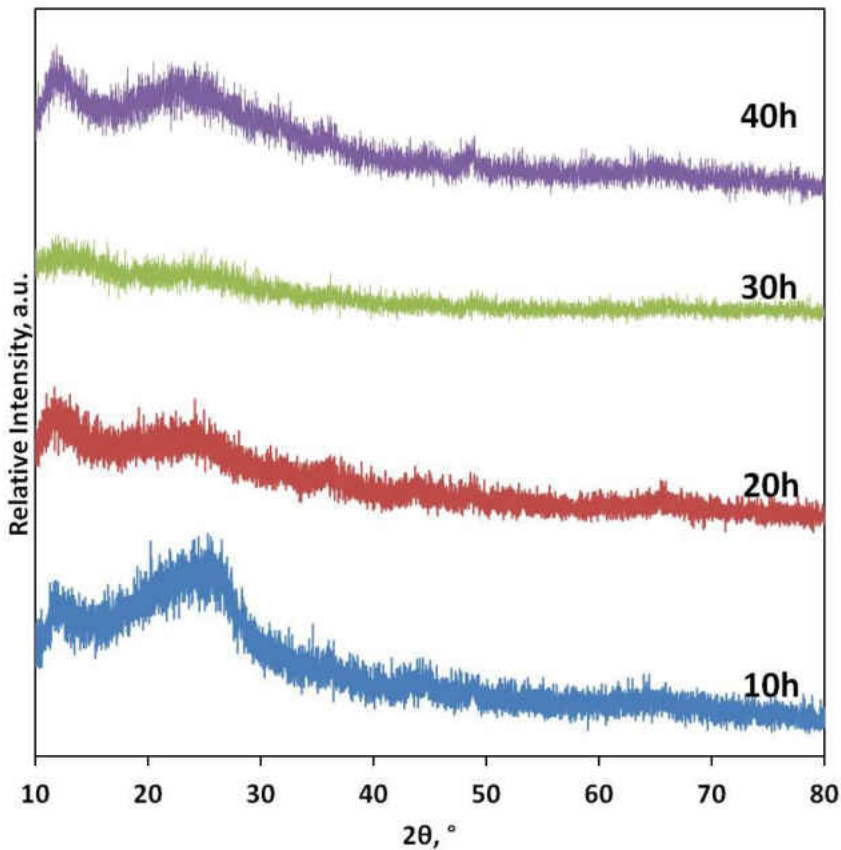


Figure 35: XRD patterns of Al, Mg and B mixture after milling (Ball to powder mass ratio 4:1).

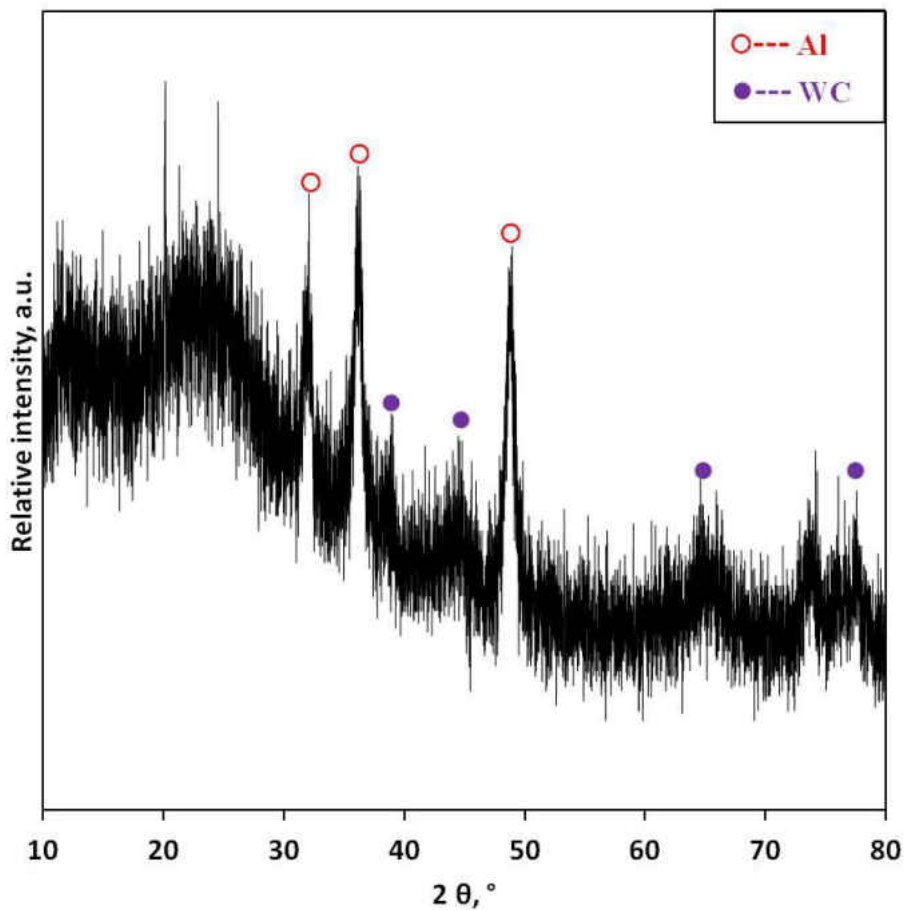


Figure 36: XRD patterns of Al, Mg and B mixture after milling (Ball to powder mass ratio 10:1).

#### 4.3.3 Experiment 3

XRD pattern of the sintered sample was shown in Figure 37. Although  $\text{MgAl}_2\text{O}_4$  still exists, the major phase was  $\text{AlMgB}_{14}$ . The first broad peak shows amorphous boron still exists. This is because the consumption of Al and Mg by oxidization and evaporation made boron left unreacted. Success of this experiment confirms the prediction that the oxidization happened



during milling in the first several experiments, but it is hard to detect  $\text{MgAl}_2\text{O}_4$  by XRD since the mixture was amorphous after the milling step.

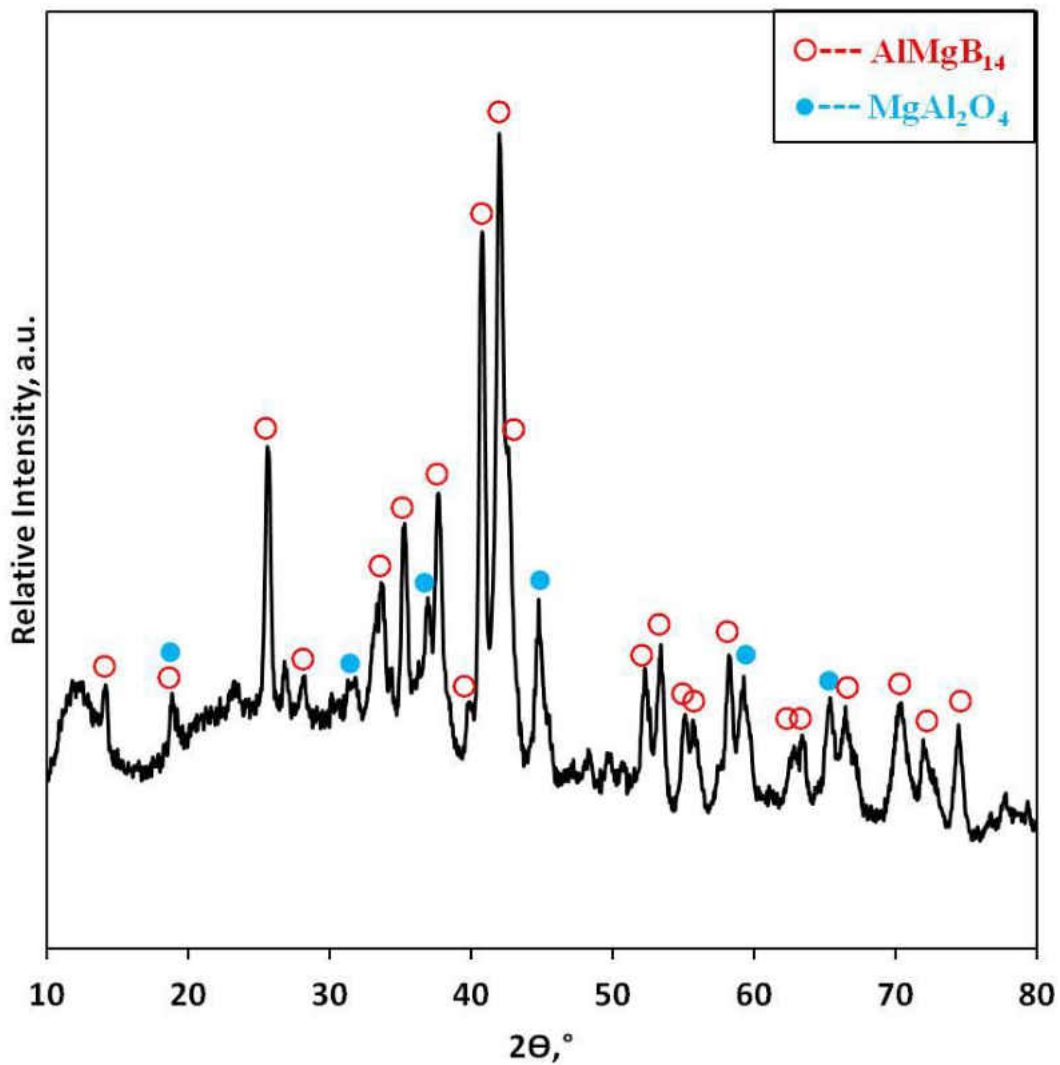
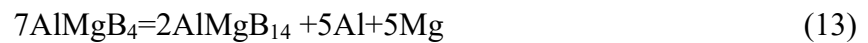


Figure 37: XRD pattern of  $\text{AlMgB}_{14}$ .

#### 4.3.4 Experiment 4

XRD patterns of the sintered samples were shown in Figure 38. Beside of the two phases usually observed  $\text{AlMgB}_{14}$  and  $\text{MgAl}_2\text{O}_4$ , the third phase  $\text{AlMgB}_4$  appeared in the sample 1, 4, 5 and 6. The  $\text{AlMgB}_4$  was also found by Roberts et al. [48] in their synthesis of  $\text{AlMgB}_{14}$  by pulse electric current. It was found that the lower boride  $\text{AlMgB}_4$  is an intermediate product. The reaction



turns  $\text{AlMgB}_4$  to  $\text{AlMgB}_{14}$  when the temperature is high enough to allow this reaction happen.

By comparing the result of Route 1 and Route 3, it can be seen that with the increasing of sintering time, the transformation rate of  $\text{AlMgB}_4$  to  $\text{AlMgB}_{14}$  increases. It shows that the longer sintering time can also make the  $\text{AlMgB}_4$  fully transformed to  $\text{AlMgB}_{14}$ . However, by comparing the result of Route 1 and Route 2, we found that the excess magnesium used in the Route 2 result in no  $\text{AlMgB}_4$  left in the sample, and the intensity of  $\text{AlMgB}_{14}$  is much higher than  $\text{MgAl}_2\text{O}_4$ . This is because Mg evaporated during sintering, while the excess Mg compensated the loss of Mg. The evaporation of Mg produces a good Mg atmosphere around the sample to prevent the oxidization of Al and Mg in the sample. This explains why this approach yields samples with the highest quality.

It shows that all the listed methods were able to produce  $\text{AlMgB}_{14}$ , even though most of them were not fully reacted to form  $\text{AlMgB}_{14}$ . It also confirmed that highly volatile pure Mg is better to be used instead of  $\text{MgB}_2$ . [49]

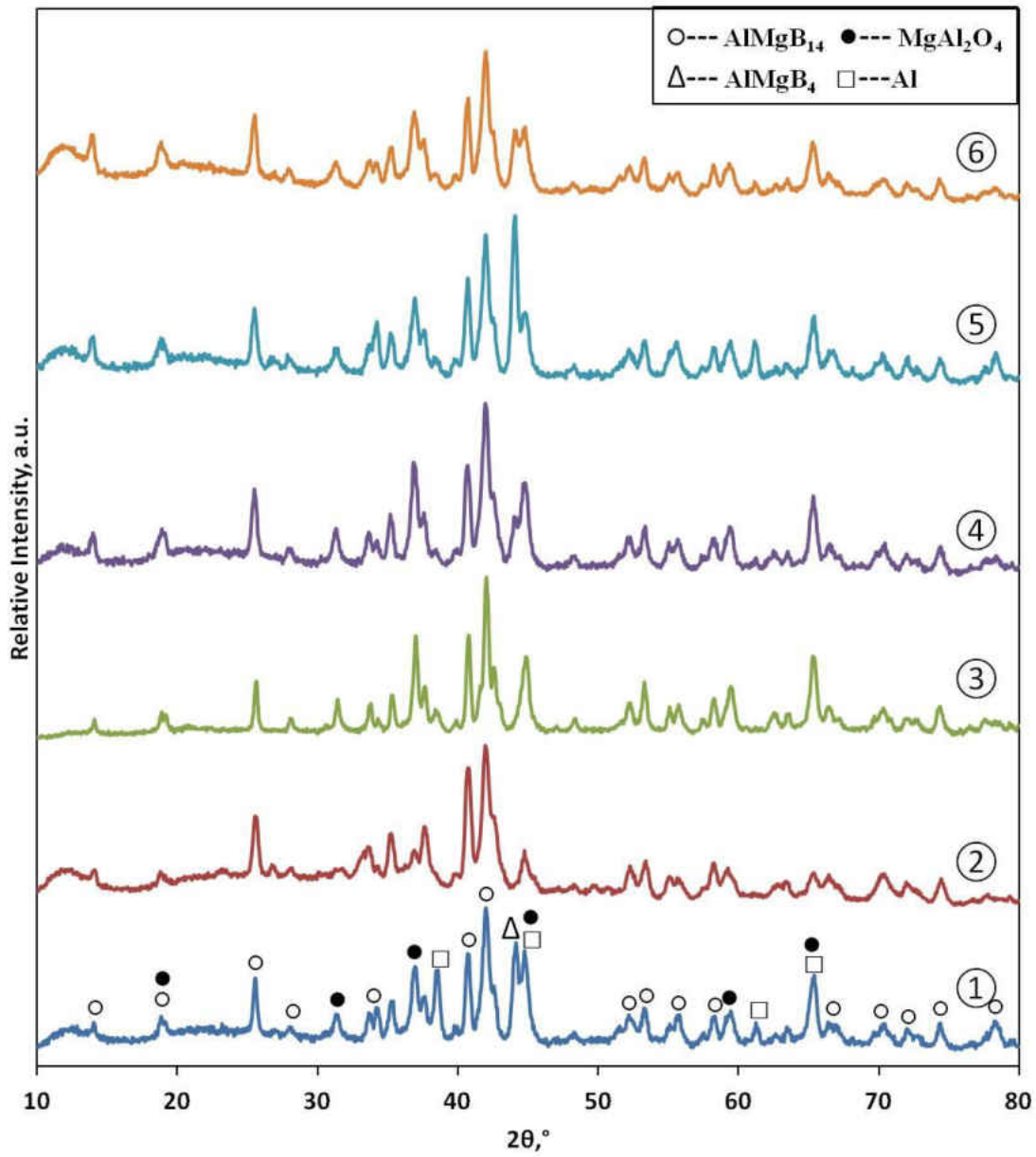


Figure 38: XRD patterns of the powder produced by different routes in experiment 4.

## CHAPTER 5: CONCLUSIONS

The synthesis of  $\text{ReB}_2$ ,  $\text{OsB}_2$  and  $\text{AlMgB}_{14}$  has been studied in this thesis. We have shown that  $\text{ReB}_2$  powders can be synthesized mechanochemically from elemental crystalline Re and amorphous B powders in the stoichiometric 1:2 ratio. A complete reaction was realized after 70-80 hours of milling in a Spex-8000 high energy ball mill. By using this approach we have eliminated the need for excess boron reported by others. The synthesized powders were agglomerates of small crystallites as evidenced by SEM. High resolution TEM showed that the material had a clear crystalline structure. The batch became contaminated both with WC-Co milling media during milling and with oxygen and hydrogen coming from the environment during selection of the intermediate samples for analysis. It is our expectation that powders free of excess of boron will facilitate a thorough understanding of the role composition on the hardness and elastic moduli of  $\text{ReB}_2$  ceramics. This is also a scalable solution that will ultimately allow larger quantities of this potentially useful material to be prepared.

The hexagonal  $\text{OsB}_2$  has been synthesized by the mechanochemical method. The 1:3 Os/B mixture powder was mill by Spex ball mill for a total of 33 hours.  $\text{OsB}_2$  starts formed after 2 hours of milling. The lattice parameters of the hexagonal  $\text{OsB}_2$  are  $a=b=2.9047 \text{ \AA}$ ,  $c=7.4500 \text{ \AA}$ ;  $\alpha=\beta=90^\circ$ ,  $\gamma=120^\circ$ . The  $\text{OsB}_2$  particle was observed by TEM, and its electron diffraction pattern was obtained. The synthesized  $\text{OsB}_2$  powder was annealed at  $1050^\circ\text{C}$  for 6 days under vacuum atmosphere. No phase change was found. This shows the hexagonal  $\text{OsB}_2$  is very stable.

The  $\text{AlMgB}_{14}$  was synthesized at  $1050^\circ\text{C}$  under normal pressure by different routes. It shows  $\text{AlMgB}_{14}$  cannot be synthesized merely by ball milling. Also, ball milling is not necessary

for the synthesis. The intermediate product  $\text{AlMgB}_4$  was found when the temperature is not high enough to turn  $\text{AlMgB}_4$  to  $\text{AlMgB}_{14}$ .  $\text{AlMgB}_{14}$  can be synthesized based on  $\text{AlB}_2$  or  $\text{MgB}_2$ , but the existence of Mg has positive effect to the synthesis.

## LIST OF REFERENCES

- [1] V. L. Solozhenko, D. Andrault, G. Fiquet, M. Mezouar, D. C. Rubie, "Synthesis of superhard cubic BC<sub>2</sub>N", *Appl. Phys. Lett.*, 78(10)(2001)1385-1387.
- [2] R. B. Kaner, J. J. Gilman, S. H. Tolbert, "Designing superhard materials", *Science*, 308(2005) 1268-1269.
- [3] R. W. Cumberland, M. B. Weinberger, J. J. Gilman, S. M. Clark, S. H. Tolbert, R. B. Kaner, "Osmium diboride, an ultra-incompressible, hard material", *J. Am. Chem. Soc.*, 127(2005) 7264-7265.
- [4] H. Y. Chung, M. B. Weinberger, J. B. Levine, A. Kavner, J. M. Yang, S. H. Tolbert, R. B. Kaner, "Synthesis of ultra-Incompressible superhard rhenium diboride at ambient pressure", *Science*, 316(5823)(2007) 436-439.
- [5] N. Orlovskaya, Z. Xie, M. Klimov, H. Heinrich, D. Restrepo, R. Blair, C. Suryanarayana, "Mechanochemical synthesis of ReB<sub>2</sub> powder", *J. Mater. Res.*, 26(21)(2011) 2772-2779.
- [6] E. Gregoryanz, C. Sanloup, M. Somayazulu, J. Badro, G. Fiquet, H. K. Mao, R. J. Hemley, "Synthesis and characterization of a binary noble metal nitride", *Nature materials*, 3(2004) 294-297.
- [7] J. C. Crowhurst, A. F. Goncharov, B. Sadigh, C. L. Evans, P. G. Morrall, J. L. Ferreira and A. J. Nelson, "Synthesis and characterization of the nitrides of platinum and rridium", *Science*, 311(2006) 1275-1278.
- [8] A. F. Young, C. Sanloup, E. Gregoryanz, S. Scandolo, R. J. Hemley, H. K. Mao, "Synthesis of novel transition metal nitrides IrN<sub>2</sub> and OsN<sub>2</sub>", *Phys. Rev. Lett.*, 96(15)(2006) 155501.
- [9] F. Ren, Y. Wang, V. C. Lo, "Pressure induced structural phase transition of OsB<sub>2</sub>: First principle calculations", *J. Solid State Chem.*, 183(4)(2010) 915-919.
- [10] H. Y. Chung, J. M. Yang, S. H. Tolbert, R. B. Kaner, "Anisotropic mechanical properties of ultra-imcompressible hard osmium diboride", *J. Mater. Res.*, 23(6)(2008) 1797-1801.
- [11] T. Mori, "Handbook on the physics and chemistry of rare earths" 38(2007) 105-173.
- [12] R. Cherukuri, M. Womack, P. Molian, A. Russell and Y. Tian, "Pulsed laser deposition of AlMgB<sub>14</sub> on carbide inserts for metal cutting", *Surf. Coat. Technol.*, 155(2002), 112-120.

- [13] A. Latini, J. V. Rau, D. Ferro, R. Teghil, V. R. Albertini, and S. M. Barinov, "Superhard rhenium diboride films: preparation and characterization", *Chem. Mater.* 20(2008) 4507-4511.
- [14] J. B. Levine, S. L. Nguyen, H. I. Rasool, J. A. Wright, S. E. Brown, and R. B. Kaner, "Preparation and properties of metallic, superhard rhenium diboride crystals", *J. Am. Chem. Soc.*, 130(2008) 16953-16958.
- [15] W. Zhou, H. Wu, and T. Yildirim "Electronic, dynamical, and thermal properties of ultra-incompressible superhard rhenium diboride: A combined first-principles and neutron scattering study", *Phys. Rev. B*, 76(2007) 184113.
- [16] S. Aydin and M. Simsek, "First-principles calculations of  $MnB_2$ ,  $TcB_2$ , and  $ReB_2$  within the  $ReB_2$ -type structure", *Phys. Rev. B*, 80(2009), 134107.
- [17] Y. Liang and B. Zhang, "Mechanical and electronic properties of superhard  $ReB_2$ ", *Phys. Rev. B*, 76(2007) 132101.
- [18] X. Q. Chen, C. L. Fu, M. Krčmar, and G. S. Painter, "Electronic and structural origin of ultraincompressibility of 5d transition-metal diborides  $MB_2$  ( $M=W, Re, Os$ )", *Phys. Rev. Lett.*, 100(2008), 196403.
- [19] J. Pellicer-Porres, A. Segura<sup>1</sup>, A. Munoz, A. Polian, and A. Congeduti, "Bond length compressibility in hard  $ReB_2$  investigated by x-ray absorption under high pressure", *J. Phys.: Condens. Matter*, 22(2010), 045701.
- [20] M. R. Koehler, V. Keppens, B. C. Sales, R. Jin, and D. Mandrus, "Elastic moduli of superhard rhenium diboride", *J. Phys. D: Appl. Phys.*, 42(2009), 095414.
- [21] S. J. LaPlaca and B. Post, "The crystal structure of rhenium diboride", *Acta Crystallogr.*, 15(1962) 97-99.
- [22] R. F. Zhang, S. Veprek, and A. S. Argon, "Mechanical and electronic properties of hard rhenium diboride of low elastic compressibility studied by first-principles calculation", *Appl. Phys. Lett.*, 91(2007) 201914.
- [23] S. Otani, T. Aizawa, Y. Ishizawa, Preparation of  $ReB_2$  single crystals by the floating zone method, *J. Alloys Compd.*, 252 (1997) L19-L21.
- [24] A. J. McAlister, "Binary alloy phase diagrams", edited by T.B. Massalski, H. Okamoto, P.R. Subramanian and L. Kacprzak (ASM International, Materials Park, OH, USA, 1990) P. 136.

- [25] S. Otani, M. M. Korsukova, and T. Aizawa, "High-temperature hardness of  $\text{ReB}_2$  single crystals", *J. Alloys Compd.*, 477(2009), L28-L29.
- [26] J. Qin, D. He, J. Wang, L. Fang, L. Lei, Y. Li, J. Hu, Z. Kou, and Y. Bi, "Is rhenium diboride a superhard material?", *Adv. Mater.* 20(2008), 4780-4783.
- [27] J. B. Levine, J. B. Betts, J. D. Garrett, S. Q. Guo, J. T. Eng, A. Miglion, and R. B. Kaner, "Full elastic tensor of a crystal of the superhard compound  $\text{ReB}_2$ ", *Acta mater.*, 58(5)(2010), 1530-1535.
- [28] B. L. Ivanov, M. S. Wellons, and C. M. Lukehart, "Confined-Plume chemical deposition: rapid synthesis of crystalline coatings of known hard or superhard materials on inorganic or organic supports by resonant IR decomposition of molecular precursors", *J. Am. Chem. Soc.*, 131(2009), 11744-11750.
- [29] A. B. Lyashchenko, V. N. Paderno, V. B. Filippov, and D. F. Borshchevskii, "Preparation and some properties of rhenium diboride monocrystals", *Sverkhtverd. Mater.*, 28(4) (2006) 72-74.
- [30] M. Frotscher, M. Holzel, and B. Z. Albert, "Crystal structures of the metal diborides  $\text{ReB}_2$ ,  $\text{RuB}_2$ , and  $\text{OsB}_2$  from neutron powder diffraction", *Z. Anorg. Allg. Chem.*, 636(2010), 1783-1786.
- [31] A. M. Locci, R. Licheri, R. Orru, and G. Cao, "Reactive spark plasma sintering of rhenium diboride ceramic", *Ceram. Int.*, 35(2009), 397-400.
- [32] N. Dubrovinskaia, L. Dubrovinsky, and V.L. Solozhenko, "Comment on 'Synthesis of ultra-incompressible superhard rhenium diboride at ambient pressure'", *Science*, 318(2007) 1550C.
- [33] H. Cynn, J. E. Klepeis, C-S. Yoo, and D. A. Young, "Osmium has the lowest experimentally determined compressibility", *Phys. Rev. Lett.*, 88(2002) 135701.
- [34] T. Kenichi, "Bulk modulus of osmium: High-pressure powder x-ray diffraction experiments under quasihydrostatic conditions", *Phys. Rev. B*, 70(2004) 012101.
- [35] L. Stuparevic and D. Zivkovic, "Phase diagram investigation and thermodynamic study of Os-B systems", *J. Therm. Anal. Calorim.*, 76(2004) 975-983.
- [36] Y. Singh, C. Martin, S. L. Bud'ko, A. Ellern, R. Prozorov, D. C. Johnston, "Multi-gap superconductivity and Shubnikov-de Haas oscillations in single crystals of the layered boride  $\text{OsB}_2$ ", *Phys. Rev. B*, 82(2010) 144532.



- [37] M. Hebbache, L. Stuparevic, D. Zivkovic, "A new superhard material Osmium diboride OsB<sub>2</sub>", *Solid State Commun.*, 139(2006) 227-231.
- [38] B. Aronsson, "The Crystal Structure of RuB<sub>2</sub>, OsB<sub>2</sub>, and IrB<sub>1.35</sub> and Some General Comments on the Crystal Chemistry of Borides in the Composition Range MeB-MeB<sub>3</sub>", *Acta Chem. Scand.*, 17 (1963) 2036-2050.
- [39] R. B. Roof and C.P. Kempter, "New orthorhombic phase in the Ru-B and Os-B systems", *J. Chem. Phys.*, 37(7)(1962) 1473-1476.
- [40] Y.X. Wang, "Elastic and electronic properties of TcB<sub>2</sub> and superhard ReB<sub>2</sub>: First-principles calculations" *Appl. Phys. Lett.* 91(10)(2007) 101904.
- [41] L. Rao, E. G. Gillan, R. B. Kaner, "Rapid synthesis of transition-metal borides by solid-state metathesis", *J. Mater. Res.*, 10(2)(1995) 353-361.
- [42] C. Li, P. Wu, "Correlation of Bulk Modulus and the Constituent Element properties of binary intermetallic compounds", *Chem. Mater.*, 13(2001) 4642-4648.
- [43] M.L. Cohen, "Predicting useful materials", *Science*, 261(1993) 307-308.
- [44] U. Lundin, L. Fast, L. Nordstrom, B. Johansson, J. M. Wills, O. Eriksson, "Transition-metal dioxides with a bulk modulus comparable to diamond", *Phys. Rev. B*, 57(1998) 4979-4982.
- [45] J. Yang, H. Sun, C. Chen, "Is osmium diboride an ultra-hard material?", *J. Am. Chem. Soc.*, 130(2008), 7200-7201.
- [46] V. I. Matkovich, J. Economy, "Structure of MgAlB<sub>14</sub> and a brief critique of structural relationship in higher borides", *Acta Cryst. B*26(1970) 616-621.
- [47] T. L. Lewis, B. A. Cook, J. L. Haring, A. M. Russell, "Al<sub>2</sub>MgO<sub>4</sub>, Fe<sub>3</sub>O<sub>4</sub>, and FeB impurities in AlMgB<sub>14</sub>", *Mater. Sci. and Eng. A*, 351(2003) 117-122.
- [48] D. J. Roberts, J. Zhao, Z. A. Munir, "Mechanism of reactive sintering of MgAlB<sub>14</sub> by pulse electric current", *Int. J. Refract. Met. Hard Mater.* 27(2009) 556-563.
- [49] V. Kevorkijan, S. D. Skapin, M. Jelen, K. Krnel, A. Meden, "Cost-effective synthesis of AlMgB<sub>14-x</sub>TiB<sub>2</sub>", *J. Eur. Ceram. Soc.* 27(2007) 493-497.
- [50] Y. Y. Sun, P. X. Zhang, G. Q. Liu, X. M. Xiong, F. Yang, G. F. Jiao, C. P. Zhang, G. Yan, "Effect of two-step heat treatment on the phase formation of MgAlB<sub>14</sub>", *Mater. Lett.*, 65(2011) 2158-2160.

- [51] I. Higashi, M. Kobayashi, S. Okada, K. Hamano, T. Lundstrom, "Boron-rich crystals in A1-M-B (M = Li, Be, Mg) systems grown from high-temperature aluminum solutions", *J. Cryst. Growth*, 128 (1-4)(1993) 1113-1119.
- [52] B. A. Cook, J. L. Harringa, T. L. Lewis, A. M. Russell, "A new class of ultra-hard materials based on AlMgB<sub>14</sub>", *Scripta mater.* 42 (2000) 597-602.
- [53] G. Kaupp, "Waste-free synthesis and production all across chemistry with the benefit of self-assembled crystal packings", *J. Phys. Org. Chem.*, 21(2008), 630-643.
- [54] J. J. Gilman, "Mechanochemistry", *Science*, 274(1996) 65.
- [55] J. J. Gilman, "Mechanism of shear-induced metallization", *Czech. J. Phys.*, 45(1995) 913-919
- [56] V. V. Boldyrev and K. Tkacova, "Mechanochemistry of Solids: Past, Present, and Prospects", *J. Mater. Synth. Process.*, 8(3/4)(2000) 121-132.
- [57] G. Heinicke, *Tribochemistry*, Akademie-Verlag, Berlin, 1984.
- [58] S. M. Hick, C. Griebel, D. T. Restrepo, J. H. Truitt, E. J. Bucker, C. Bylda and R. G. Blair, "Mechanocatalysis for biomass-derived chemicals and fuels" *Green Chem.*, 12(2010) 468-474.
- [59] C. Suryanarayana: *Mechanical alloying and milling*. *Prog. Mater.Sci.* 46, 1 (2001).
- [60] C. Suryanarayana: *Mechanical alloying and milling*. (Marcel Dekker, Inc., New York, NY, 2004), pp. 466.
- [61] L. Takacs, "Self-sustaining reactions induced by ball milling", *Prog. Mater. Sci.*, 47(2002) 355-414.
- [62] W. Haessler, O. Perner, C. Fischer, K. Nenkov, C. Rodig, M. Schubert, M. Herrmann, L. Schultz, B. Holzapfel, and J. Eckert, "Superconducting MgB<sub>2</sub> tapes prepared using mechanically alloyed nanocrystalline precursor powder", *Appl. Supercond.*, 17(2) (2007) 2919-2921.
- [63] Y. Hwang and J. K. Lee, "Preparation of TiB<sub>2</sub> powders by mechanical alloying", *Mater. Lett.*, 54(2002) 1-7.
- [64] P. Millet and T. Hwang, "Preparation of TiB<sub>2</sub> and ZrB<sub>2</sub>. influence of a mechanochemical treatment on the borothermic reduction of titania and zirconia", *J. Mater. Sci.*, 31(2)(1996) 351-355.

- [65] D. D. Radev and D. Klisurski, "Properties of TiB<sub>2</sub> powders obtained in a mechanochemical way", *J. Alloys Compd.*, 206(1)(1994) 39-41.
- [66] N. Setoudeh and N. J. Welham, "Formation of zirconium diboride (ZrB<sub>2</sub>) by room temperature mechanochemical reaction between ZrO<sub>2</sub>, B<sub>2</sub>O<sub>3</sub> and Mg", *J. Alloys Compd.*, 420(2006) 225-228.
- [67] R. A. Varin and C. Chiu, "Synthesis of nanocrystalline magnesium diboride (MgB<sub>2</sub>) metallic superconductor by mechano-chemical reaction and post-annealing", *J. Alloys Compd.*, 407(2006) 268-273.
- [68] D. J. Gardiner (1989). *Practical Raman spectroscopy*. Springer-Verlag. ISBN 978-0387502540.
- [69] G. E. Boyd, J. W. Cobble, and W.T. Smith, "Thermodynamic properties of technetium and rhenium compounds. III. heats of formation of rhenium heptoxide and trioxide, and a revised potential diagram for rhenium", *J. Am. Chem. Soc.*, 75(1953) 5783.
- [70] S. V. Meschel and O. J. Kleppa, "Standard Enthalpies of Formation of NbB<sub>2</sub>, MoB, and ReB<sub>2</sub> by High-Temperature Direct Synthesis Calorimetry", *Metall. Mater. Trans. A*, 24(1993) 947.
- [71] A. C. Larson and R. B. Von Dreele, "General Structure Analysis System (GSAS)", Los Alamos National Laboratory Report LAUR 86-748 (1994)
- [72] B. H. Toby, "EXPGUI, a graphical user interface for GSAS", *J. Appl. Cryst.*, 34(2001), 210-213
- [73] V. V. Boldyrev, *J. Chem. Phys.*, 83, 821 (1986).